Experimental and Numerical Study on Performance of Open Cross-Flow Hydraulic Turbine

March, 2022

Tianbo WANG

A THESIS SUBMITTED TO THE FACULTY OF

GRADUATES STUDIES

IN PARTIAL FULFILMENT OF THE

REQUIREMENTS FOR THE

DEGREE OF DOCTOR OF PHILOSOPHY

PhD (2022) Niigata University

(Mechanical engineering)

TITLE : Experimental and Numerical Study on Performance of Open Cross-Flow Hydraulic Turbine

Author : Tianbo WANG

Supervisor(s) : Professor N. Fujisawa

Professor K. Hiramoto

Number of pages : 82

Experimental and Numerical Study on Performance of Open Cross-Flow Hydraulic Turbine

ABSTRACT

The flow and torque mechanisms of an open cross-flow hydraulic turbine in underflow and waterfall conditions are investigated through experiments and numerical simulations. The unsteady flow fields around a hydraulic turbine are measured by a phase-averaged particle image velocimetry in an open-circuit water tunnel, and the results are compared with those of a two-dimensional numerical simulation using the volume of fluid method for two-phase flow analysis. The experimental and numerical results of the flow fields generally agree well with each other in both operating condition, suggesting the validity of the two-dimensional numerical simulation for open cross-flow hydraulic turbines.

In underflow operating condition, the experimental and numerical results indicate that both the accelerated flows over the downstream blade and through the bottom spacing between the turbine and channel wall yielded the positive torque generation of the cross-flow turbine. It is discovered that these flow features improved by decreasing the bottom spacing, and that they contributed to the local torque generation; consequently, the torque performance and efficiency of the cross-flow turbine improved. However, very small bottom spacing may not be effective for improving the efficiency. The maximum efficiency attains 39%, when the bottom spacing is optimized.

In waterfall operating condition, the experimental and numerical results indicate that the flow and torque mechanisms of the cross-flow hydraulic turbine studied are explained by stagnation pressure on the concave side of blades and a Coanda-like flow on the convex side of the blades at small angle of blade position, followed by the formation of a high-velocity region within the turbine and flow impingement on the downstream blades at large angle. These flow field variations generated an increased local torque at small angle and a moderate torque at large angle, and the maximum efficiency reached approximately 60%, which is higher than that of the underflow operating condition. The improved efficiency was obtained by optimizing the off-axis distance to the waterfall and the tip-speed ratio of the hydraulic turbine, which were verified by a visualization of the flow through the turbine and the local torque distribution with respect to the angle of blade position, respectively.

Table of contents

List of figures

List of tables

Nomenclature

C : chord length [mm]

C_p : pressure coefficient [-]

C_t : torque coefficient [-]

$C_{t\theta}$: blade-averaged torque coefficient [-]

$C_{t\theta}'$: local torque coefficient [-]

C_μ : empirical constant [-]

$C_{\varepsilon 1}$: empirical constant [-]

$C_{\varepsilon 2}$: empirical constant [-]

D_i : inner diameter [mm]

D_o : outer diameter [mm]

f_σ : surface tension [N/m]

g : gravitational acceleration [m^2/s]

H : water head [m]

He : nozzle exit height [m]

H_b : bottom spacing [mm]

H_d : downstream water level [mm]

H_u : upstream water level [mm]

ΔH: the water level difference between upstream and downstream (= H_u - H_d) [mm]

k : Turbulent kinetic energy [m^2/s^2]

L : off-axis distance [mm]

P : pressure [pa]

p_1 : pressure on the concave side [pa]

p_2 : pressure on the convex side [pa]

Q : flow rate [m^3/s]

r : radial distance [m]

R : radius of turbine ($=D_o/2$) [m]

R_1 : blade radius [m]

t : time [s]

T : torque [Nm]

U : mean velocities in x- directions [m/s]

U_0 : free-stream velocity [m/s]

U_e : mean velocity at nozzle exit [m/s]

U_d : downstream velocity [m/s]

U_m : velocity magnitude [m/s]

V : mean velocities in y-directions [m/s]

W : width of turbine [mm]

x : streamwise coordinate [mm]

y : normal coordinate [mm]

z : spanwise coordinate [mm]

β_i : inlet angle [°]

β_o : outlet angle [°]

δ : Kronecker delta [-]

ε : dissipation rate [m^2/s^3]

η : efficiency (= $T\omega/(\rho gQH)$) [-]

η_{max} : maximum efficiency [-]

$\eta_{\Delta H}$:efficiency calculated by ΔH (= $T\omega/(\rho gQ\Delta H)$) [-]

θ : measured angle [°]

θ_b : blade angle [°]

λ : tip-speed ratio (= $D_o\omega/2U_o$) [-]

ν_t : turbulent viscosity [m^2/s]

ρ : density of water [kg/m^3]

σ_k : empirical constant [-]

σ_ε : empirical constant [-]

φ : angle [°] (see Fig. 2-1)

ω : angular velocity [rad/s]

Chapter 1 Introduction

1.1 Background

Against the background of the reduction of non-renewable resources and environmental problems in the world today, the development of renewable resources has become an important issue in the energy field. The current common new renewable energy resources mainly include hydropower, wind power, solar energy and tidal power. Compared to wind power, solar energy and tidal power, the hydropower has more advantages in terms of equipment cost, application condition and safe production. Therefore, vigorously developing hydropower generation is the focus of today's energy application field. The basic principle of hydropower generation is to use the gravitational potential energy generated by the water head to drive the turbine, convert the potential energy into the kinetic energy of waterwheel, and drive the generator to rotate to generate electricity (Fatemeh et al.,2016).

Hydraulic turbines are divided into two groups based on the principle of operation: reaction turbines and impulse turbines. Reaction turbines are acted on by water, which changes as it moves through the turbine and converts the energy, such as Propeller, Francis turbine and pump-as-turbine. Impulse turbines are driven by the water jet, which pushes on the turbine's curved blades and changes the direction of the flow. Pelton, Turgo and Cross flow turbines are classified as impulse turbines. However, different types of turbines are suitable for different head and flow conditions. Fig.1-1 show the turbine selection chart based on head and flow rate (Uhunmwangho et al., 2018). In a Pelton turbine, water jets from nozzles strike the double cupped buckets attached to the wheel, cause a force that rotates the wheel at high efficiency rates. Pelton turbines are suited for high head, low flow applications. Turgo turbines are commonly used as high and

medium head impulse turbines. A Francis turbine has a radial or mixed radial or axial flow runner which is most mounted in a spiral casing with internal adjustable guide vanes (Elbatran et al., 2015). Table 1-1 shows the classification of small hydropower schemes based on the water head. In the class of impulse turbine, most types of turbines are suitable for conditions with high and medium head. On the other hand, reaction turbines are more suitable in medium and low head (Uhunmwangho et al., 2018).

Compared with other impulse turbine types, cross-flow hydraulic turbine is more suitable in the medium and low head and flow rate conditions. Unlike most water turbines where the fluid flows in radially or axially, the fluid passes directly through the side of the cross-flow hydraulic turbine or directly through the turbine blades. An example of the cross-sectional geometry of cross-flow hydraulic turbine is shown in Fig.1-2, which has 25 blades (Adhikari & Wood, 2018a). The water flow enters from the nozzle, after flowing into the runner, the fluid will flow out from the opposite side of the turbine. This design will cause the fluid to flow through the runner twice, thereby gaining additional benefits. So, the kind of hydraulic turbine has better annual operation efficiency in small rivers and seasonal rivers. In addition, the cross-flow hydraulic turbine has the advantages of low cost, sample maintenance and cleaning (Elbatran et al.,2015). The turbine shown in the Figure 1-3 is a closed cross-flow hydraulic turbine, which consists of several components, include inlet tube, guide vane, runner, casing and so on. In the turbine, the fluid will flow in a closed space (Myin & Nyi, 2018).

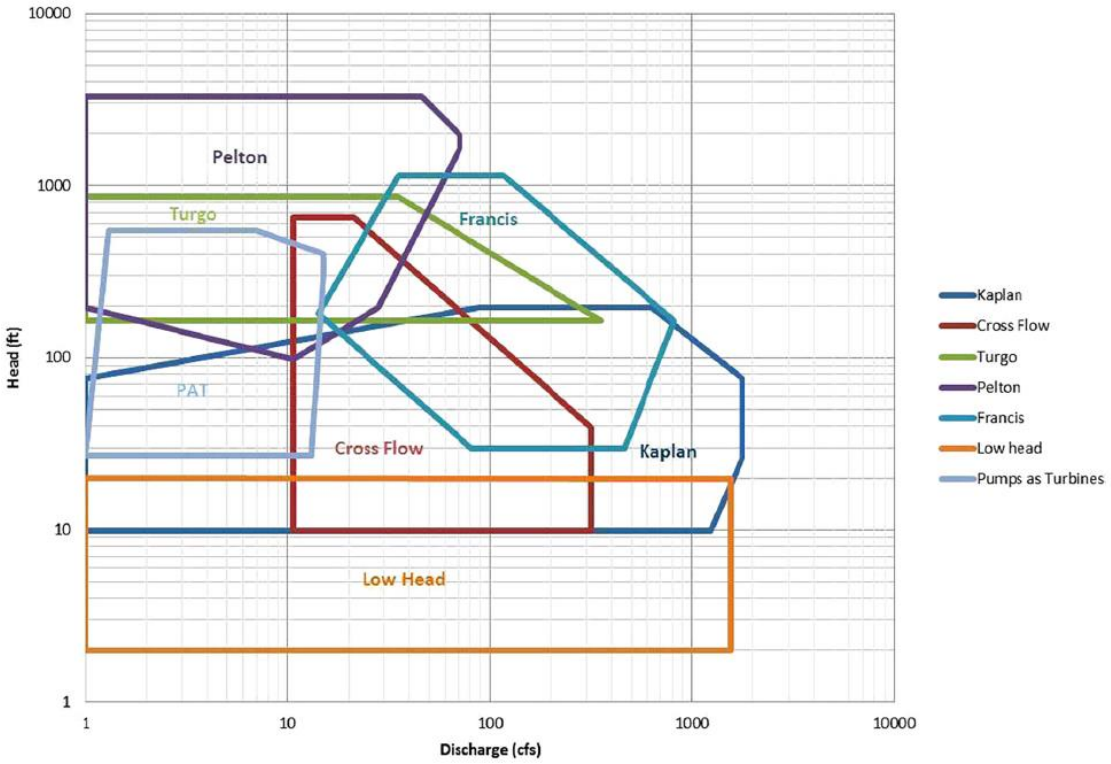

Fig.1-1 Turbine selection chart based on head and flow rate (Uhunmwangho et al., 2018).

Table 1-1 Classification of small hydropower schemes (Uhunmwangho et al., 2018).

Turbine runner	Head classification		
	High (above 50m or 160 ft)	Medium (10-50 m or 32 ft - 160 ft)	Low (below 10m or 32 ft)
Impulse	Peton	Cross flow	Cross flow
	Turgo	Turbo	
	Multi-jet Pelton	Multi-jet Pelton	
Reaction		Francis (Spiral Case)	Propeller
		Kaplan	Kaplan
		Pump-as-Turbine (PAT)	Francis (Open-flume)

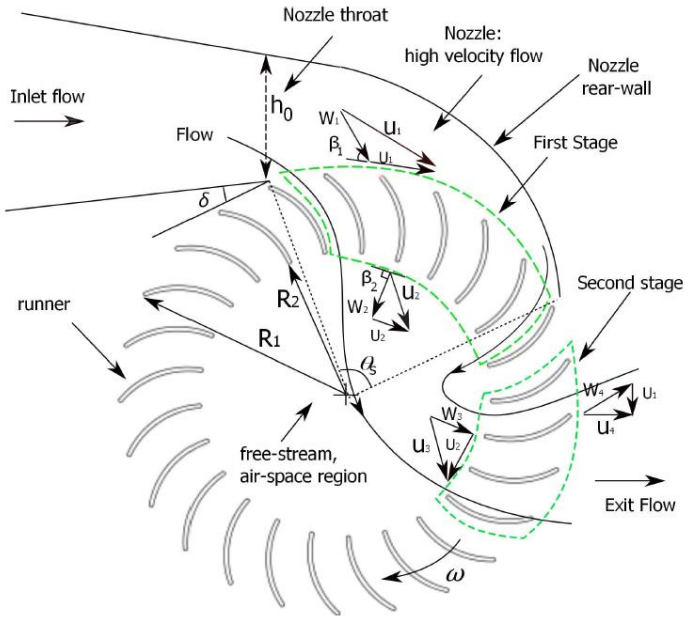

Fig.1-2 Cross-section of the cross-flow hydraulic turbine (Adhikari et al.,2018a).

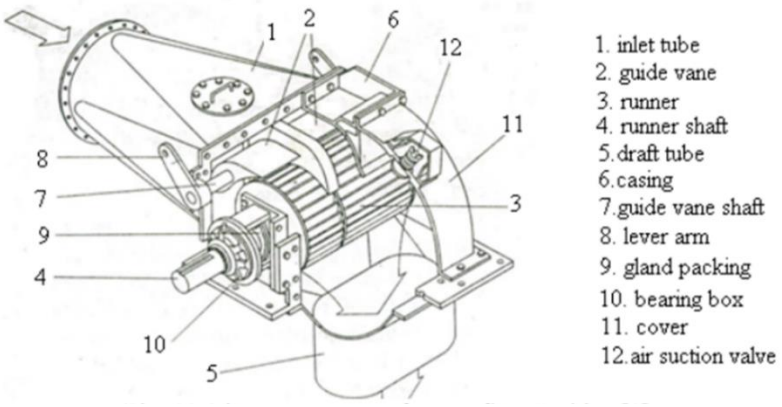

Fig.1-3 The cross-flow hydraulic turbine and its parts (Myin & Nyi, 2018).

Compared with closed cross-flow hydraulic turbine, the open cross-flow turbines are more suitable for application in underdeveloped areas. Because the open cross-flow turbines have less components, without guide vane, inlet tube, casing and so on. Figure 1-3 shows the horizontal application of the open cross-flow hydraulic turbine. Figure 1-4 shows the vertical application

of the open cross-flow hydraulic turbine. The hydraulic turbine is applied in rural area. Use the water flow from agricultural channels, flood canals, water and sewage facilities and so on to drive turbine. And the turbine generate electrician to use for the lighting of nearby roads, management lights, electric fences, and so on (Ministry of Agriculture, Forestry and Fisheries. Ishida, M., 2015).

Fig.1-4 The horizontal application of the cross-flow hydraulic turbine (Ministry of Agriculture, Forestry and Fisheries).

Fig.1-5 The vertical application of the cross-flow hydraulic turbine (Ishida, M.).

1.2 Recent research

1.2.1 Cross-flow hydraulic turbines

In recent years, research regarding microscale hydropower generation systems has increased because of the increased importance of electric power generation in rural areas. Such a system should incur low manufacturing costs and be easily maintained from the industrial perspective. Cross-flow hydraulic turbines have garnered attention as power generation systems in rural areas of developing countries because of their reasonable efficiency and the potentially low manufacturing cost of the system compared with those of other types of turbines, such as the Pelton and Francis turbines (Kahn et al., 2009; Vermaak et al., 2014).

Cross-flow hydraulic turbines can be categorized into closed and open types depending on the presence of an enclosure around the turbine. A closed-type cross-flow hydraulic turbine was designed for high performance using a casing and nozzle. The maximum efficiency achieved by closed-type cross-flow hydraulic turbines ranged from 66 % to 92 %. The large divergence in experimental efficiencies recorded could be caused by various design parameters such as the number of blades, diameter ratio of the turbines, blade angles, aspect ratio, casing, and nozzle geometry. The cross-flow hydraulic turbines have been studied both experimentally and numerically. The experimental and computational studies relevant to the design of high efficiency cross-flow turbine have been reviewed. The fundamental design principles are outlined that the total conversion of head into kinetic energy in the nozzle and the matching of nozzle and runner designs are the two main design requirements, and the key parameters are recommended based on the design of the most efficient closed-type cross-flow hydraulic turbine. These parameters include runner radius ratio, outer and inner blade angles, entry arc angle, the number of blades, nozzle aspect ratio and nozzle geometry (Adhikari & Wood, 2018a).

Several studies have been conducted to improve the efficiency of closed cross-flow hydraulic turbines (Mockmore and Merryfield, 1949; Nakase et al., 1982; Khosrowpanah et al., 1988; Fukutomi et al., 1991, 1995; Desai et al., 1994; Costa Pereira & Borges, 1996). Furthermore, optimization studies have been performed using numerical simulations based on computational fluid dynamics (Choi et al., 2008; De Andrade et al., 2011; Sammartano et al., 2013, 2015, 2016; Acharya et al., 2015; Sinagra et al., 2016; Adhikari & Wood, 2017, 2018b), These results indicated that the maximum efficiency ranged from 69 % to 86 %, which was comparable to the experimental maximum efficiency of 66 % to 92% in the literature. Thus, these studies show that the performance of closed cross-flow hydraulic turbines could be reproduced well by numerical simulations.

In recent years, optimization of the design parameters of closed cross-flow hydraulic turbines has been investigated using numerical simulations with the aid of the volume of fluid (VOF) method for two-phase flow analysis. The relations not only between the performance and internal flow of a cross-flow turbine model, but also between velocity and pressure distributions at the flow passage are examined with the variation of nozzle shape, blade angle and blade number using CFD analysis. Pressure and velocity in the flow passage of the cross-flow turbine change simultaneously with the variation of the turbine structure. Among the turbine structures examined nozzle shape gives largest effect on the turbine performance and internal flow. Output power evaluated locally from calculated pressure distribution on the runner blade is analyzed by CFD in order to examine the effect of air layer in the turbine runner on the turbine performance. The existence of air layer improves the turbine efficiency not only from the suppression of collision loss between the runner passage flow and shaft, but also from the elimination of loss by recirculating flow in the runner passage (Choi et al., 2008).

1.2.2 Open-type cross-flow hydraulic turbines

Open cross-flow hydraulic turbines without surrounding enclosures have been less studied in the literature in comparison with closed designs. The primary advantage of open cross-flow hydraulic-turbine designs is easy maintenance of the power generation system, and the lack of a requirement of a trash rack for remote operation. Thus, such systems are more suitable for application to microgeneration systems in rural areas. However, the power efficiency of open cross-flow hydraulic turbines is lower than that of the closed designs in the present state of the art. This may be due to the influence of the surrounding enclosure, including the free-surface effect; however, the reason is as yet not fully understood, as a result of fewer studies having been performed on this type of hydraulic turbine.

Meanwhile, the open cross-flow hydraulic turbine is characterized by a simple structure without enclosure; it is ideal for microscale hydro power generation systems in rural areas because of its low manufacturing cost and easy maintenance compared with the closed type. It is noteworthy that other open-type hydraulic converters exist, such as the Sagebien and Zuppinger waterwheels, whose geometries are similar to those of cross-flow hydraulic turbines; however, operate more slowly with a high energy conversion efficiency (Senior et al., 2010; Quaranta & Müller, 2018).

To increase the performance of the small turbines that combine efficiency and economy, many scholars have been focusing on the shape of the turbine blade. They have been using the numerical analysis methods to design, simulate and improve the shape and using experimental method to test the design. For example, Vincenzo et al. (2013) report that Banki-michell optimal design by computational fluid dynamics testing and hydrodynamic analysis. After they have reviewed the available criteria for Banki-Michell parameter design, describe a novel two-step procedure. In the first step, the initial and final blade angles, the outer impeller diameter and the

shape of the nozzle are selected using a simple hydrodynamic analysis, based on a very strong simplification of reality. In the second step, the inner diameter, as well as the number of blades and their shape, are selected by testing single options using computational fluid dynamics (CFD) simulations, starting from the suggested literature values. Good efficiency is attained not only for the design discharge, but also for a large range of variability around the design value (Sinagra et al.,2016).

The previous studies on open cross-flow hydraulic turbines include designs that can be categorized as underflow and waterfall types, depending on the flow direction against the hydraulic turbine.

Nishi et al. (2013) focus on studies of the undershot cross-flow water turbine in open channels. A water turbine suitable for ultra-low heads in open channels is developed, with the end goal being the effective utilization of unutilized hydroelectric energy in agricultural water channels. And they perform tests by applying a cross-flow runner to an open channel as an undershot water turbine while attempting to simplify the structure and eliminate the casing. They experimentally investigated the flow fields and performance of water turbines in states where the flow rate is constant for the undershot cross-flow water turbine after attaching a bottom plate to the runner. From the results, it is clarified that although the effective head for cross-flow runners with no bottom plate is lower than those found in existing runners equipped with a bottom plate, the power output is greater in the high rotational speed range because of the high turbine efficiency. It is also proved that the runner with no bottom plate differed from runners that had a bottom plate in that no water was being wound up by the blades or retained between the blades, and the former received twice the flow due to the flow-through effect. As a result, the turbine efficiency is greater for runners with no bottom plate in the full rotational speed range compared with that found in runners that had a bottom plate.

Furthermore, Nishi et al. (2014) study the flow field of undershot cross-flow water turbines by particle image velocimetry (PIV) measurements and numerical analysis methods. And the performance of this turbine and the flow field are evaluated through experiments and numerical analysis. The experimental results reflecting the performance of this turbine and the flow field are consistent with numerical analysis. In addition, the flow fields at the inlet and outlet regions at the first and second stages of this water turbine are clarified.

Recently, Iio et al. (2012) reports the study on a waterfall type hydraulic turbine investigation of a flow direction control method by using a curved channel. It is found that performance of open type cross-flow runner utilizing waterfall is strongly affected by flow imping position. Using curved channel controls the fall direction to obvious the impact from flow impinging position by flow visualization and runner performance measurement methods. As a result, it is clarified that the flow direction control method was effective to keep a stable generation when the flow rate changed widely. Namely, the adjustment of runner positions is not necessary even when the flow rate changes. This is an extreme advantage from a practical application viewpoint.

Uchiyama et al. (2015 ,2017) carried out the study that simulated the flow through a small-scale open cross-flow hydraulic turbine and analyzed the turbine's performance in waterfall operation condition. Using a two-dimensional particle method, the waterfall cross-flow hydraulic turbine was successfully simulated numerically. Flow in the turbine is successfully simulated. And the simulated turbine performance was in good agreement with experimental measurements. The simulation also clarified that the deterioration in performance with increasing water flow rate is caused by the degeneration of the radially outward flow between the rotor blades.

1.3 Purpose of this research

In the present thesis, the performance of the cross-flow hydraulic turbine in two different operations that are an underflow operation and a waterfall operation were studied by numerical and experimental methods.

In chapter 2, experimental and numerical studies of the flow around an open cross-flow hydraulic turbine in an underflow operation were conducted to analyze the torque mechanism of the hydraulic turbine. The unsteady flow field in and around the hydraulic turbine was measured via phase-averaged PIV, and the corresponding torque mechanism was investigated via two-dimensional numerical simulation based on the VOF method. The effects of the bottom spacing below the hydraulic turbine and the channel wall in improving the performance of the open cross-flow hydraulic turbine were considered.

In chapter 3, the performance of the waterfall-type cross-flow hydraulic turbine both experimentally and numerically under the condition of two-dimensional waterfall is investigated. To validate the numerical approach using the two-dimensional VOF method, the two-dimensional flow experiment is carried out by measuring the torque and power efficiency of the waterfall-type cross-flow hydraulic turbine. Furthermore, the measurements of mean velocity field in and around the hydraulic turbine are performed by the phase-averaged PIV to compare with that of the numerical simulations. Then, the torque mechanism of the waterfall-type cross-flow hydraulic turbine is elucidated based on the flow fields measurement and the numerical local torque distributions of the hydraulic turbine with respect to the blade angle variations.

Chapter 4 is the conclusion of this thesis, and the torque mechanism of the cross-flow hydraulic turbine in an underflow operation is described in relation to the bottom spacing below the hydraulic turbine, and the performance of the waterfall-type cross-flow hydraulic turbine is impacted on the location of fall water.

References

Acharya, N., Kim, C.-G., Thapa, B., & Lee, Y.-H. (2015) Numerical analysis and performance enhancement of a cross-flow hydro turbine. Renewable Energy, 80, 819-826.

Adhikari, R.C., & Wood, D. (2017) A new nozzle design methodology for high efficiency crossflow hydro turbines. Energy for Sustainable Development, 41, 139–148.

Adhikari, R.C., & Wood, D. (2018a) The design of high efficiency crossflow hydro turbines: a review and extension. Energies, 267; doi:10.3390/en11020267.

Adhikari, R.C., & Wood, D. (2018b) Computational analysis of part-load flow control for crossflow hydro-turbines. Energy for Sustainable Development, 45, 38-45.

Choi, Y.-D., Lim, J.-I., Kim, Y.-T., & Lee, Y.H. (2008) Performance and internal flow characteristics of a cross-flow hydro turbine by the shapes of nozzle and runner blade. Journal of Fluid Science and Technology, 3, 398-409.

Costa Pereira, N.H., & Borges, J.E. (1996) Study of the nozzle flow in a cross-flow turbine. International Journal of Mechanical Science, 38, 283-302.

De Andrade, J., Curiel, C., Kenyery, F., Aguillon, D., Vasquez, A., & Asuaje, M. (2011) Numerical investigation of the internal flow in a Banki turbine. International Journal of Rotating Machinery, ID841214 (12 pages).

Desai, V.R., & Aziz, N.M. (1994) An experimental investigation of cross-flow turbine efficiency. Journal of Fluid Engineering, 116, 545–550.

Elbatran, A.H., Mohamed, W. A., Yaakob, O.B., Ahmed, Y.M., & Ismail, M. A. (2015) Hydro power and turbine systems reviews. Jurnal Teknologi, 74, 83-90.

Fatemeh, B., Mehdi, N., Adi, M., & Yasser, M. A. (2016) Global renewable energy and its potential in Malaysia: A review of Hydrokinetic turbine technology. Renewable and Sustainable Energy Reviews, 62, 1270-1281.

Fukutomi, J., Senoo, Y., & Nakase, Y. (1991) A numerical method of flow through cross-flow runner. JSME International Journal, 34, 44-51.

Fukutomi, J., Nakase, Y., Ichimiya, M., & Ebisu, H. (1995) Unsteady fluid forces on a blade in a cross-flow turbine. JSME International Journal, 38, 404-410.

Iio, S., Ooike, S., Yamazaki, M., Kimoto, K., Katayama, Y., & Ikeda, T. (2012) Study on a waterfall type hydraulic turbine (Investigation of a flow direction control method by using a curved channel). *Turbomachinery*. 40, 745–753. (in Japanese)

Ishida, M. (2015) ‘‘A simple water turbine generator for agricultural canals that protects agricultural land from wild boars with small hydroelectric power generation”, Smart Japan, https://www.itmedia.co.jp/smartjapan/articles/1506/18/news020.html. (Reference date 2021,11,30) (In Japanese).

Khan, M.J., Bhuyan, G., Iqbal, M.T., & Quaicoe, J.E. (2009) Hydrokinetic energy conversion systems and assessment of horizontal and vertical axis turbines for river and tidal applications: A technology status review. Applied Energy, 86, 1823–1835.

Khosrowpanah, S., Fiuzat, A.A., & Albertson, M.L. (1988) Experimental study of cross-flow turbine. Journal of Hydraulic Engineering, 114, 299-314.

Ministry of Agriculture, Forestry and Fisheries. “Research result report”, Ministry of Agriculture, Forestry and Fisheries, https://www.maff.go.jp/j/nousin/sekkei/kanmin/pdf/ka061_02.pdf. (Reference date 2021,11,30) (In Japanese).

Mockmore, C.A., & Merryfield, F. (1949) The Banki Water Turbine. Engineering Experiment Station Bulletin Series No.25, Oregon State College, Corvallis, OR.

Myin, S.,& Nyi, N.(2018) Design of cross flow turbine and analysis of runner's dimensions on various head and flow rate. International Journal of Scientific and Research Publications, 8, 586-593.

Nakase, Y., Fukutomi, J., Watanabe, T., Suetsugu, T., & Kubota, T. (1982) A Study of cross-flow turbine, effects of nozzle shape on its performance. Small Hydro Power Fluid Machinery, ASME Winter Annual Meeting of the ASME, Phoenix, AZ, 13-18.

Nishi, Y., Inagaki, T, Omiya, R., & Fukutomi, J. (2013) Performance and internal flow of an undershot-type cross-flow water turbine. The Japan Society of Mechanical Engineers, No.2012-JBR-0906 (in Japanese).

Nishi, Y., Inagaki, T., Li, Y., Omiya, R., & Fukutomi, J. (2014a) Study on an undershot cross-flow water turbine. Journal of Thermal Science, 23, 239-245.

Nishi, Y., Inagaki, T., Li, Y., Omiya, R., & Hatano, K. (2014b) The flow field of undershot cross-flow water turbines based on PIV measurements and numerical analysis. International Journal of Fluid Machinery System, 7, 174-182.

Nishi, Y., Inagaki, T., Li, Y., Omiya, R., & Hatano, K. (2015) Study on an undershot cross-flow water turbine with straight blades. International Journal of Rotating Machinery Volume 2015, Article ID 817926, 10 pages.

Nishi, Y., Hatano, K., & Inagaki, T. (2017) Study on performance and flow field of an undershot cross-flow water turbine comprising different number of blades. Journal of Thermal Science, 26, 413–420.

Quaranta, E., & Müller, G. (2018) Sagebien and Zuppinger water wheels for very low head hydropower applications. Journal of Hydraulic Research, 56, 526-536.

Sammartano, V., Aricò, C., Carravetta, A., Fecarotta, O., & Tucciarelli, T. (2013) Banki-Michell optimal design by computational fluid dynamics testing and hydrodynamic analysis. Energies 6, 2362-2385.

Sammartano, V., Aricò, C., Sinagra, M., & Tucciarelli, T. (2015) Cross-flow turbine design for energy production and discharge regulation. Journal of Hydraulic Engineering, 141, doi :10. I 061 /(ASCE)HY. 1943 -7900.0000977.

Sammartano, V., Morreale, G., Sinagra, M., & Tucciareli, T. (2016) Numerical and experimental investigation of a cross-flow water turbine. Journal of Hydraulic Research, 54, 321-331.

Senior, J., Saenger, N., & Müller, G. (2010) New hydropower converters for very low-head differences. Journal of Hydraulic Research, 48, 703-714.

Sinagra, M., Sammartano, V., Aricò, C., & Collura, A. (2016) Experimental and numerical analysis of a cross-flow turbine. Journal of Hydraulic Engineering, 142, ID04015040 (8 pages).

Uchiyama, T., Uehara, S., Fukuhara, H., Iio, S., & Ikeda, T. (2015) Numerical study on the flow and performance of an open cross-flow mini-hydraulic turbine. Proceedings of the IMechE Part A, Journal of Power and Energy, 229, 968-977.

Uhunmwangho, R., Odje, M., & Okedu, K. E. (2018) Comparative analysis of mini hydro turbines for Bumaji Stream, Boki, Cross River State, Nigeria. Sustainable Energy Technologies and Assessments, 27, 102-108.

Vermaak, H.J., Kusakana, K., & Koko, S.P. (2014) Status of micro-hydrokinetic river technology in rural applications: A review of literature, Renewable and Sustainable Energy Reviews, 29, 625–633.

Chapter 2 Experimental and numerical studies on the performance of underflow-type cross-flow hydraulic turbine

2.1 Introduction

The open cross-flow hydraulic turbines generally work under two common flow operation conditions, namely underflow and waterfall. When a turbine work in underflow operation, it must be put into river or water channel. The water flow will flow into the turbine along the horizontal direction and turn the turbine to create torque.

Recently, researches focused on open cross-flow hydraulic turbine in underflow operation are increasing. The performance of an open cross-flow hydraulic turbine in underflow operations was investigated by Nishi et al. (2014a,b), who measured the torque performance and efficiency of a turbine located near a channel wall with a very small bottom spacing of 5mm. The outer and inner diameters of the test turbine were 180 and 120 mm, respectively, and the width of the turbine comprising 24 circular blades was 240 mm. They also performed a numerical simulation of the turbine using the volume of fluid (VOF) method to perform two-phase flow computation. Their experimental and numerical results agreed qualitatively with each other; however, a substantial difference was discovered in the peak efficiency, i.e., it was 0.23 and 0.29 in the experiment and numerical simulation, respectively. They measured the mean velocity distributions at the inlet and outlet of the blade passage using particle image velocimetry (PIV) to analyze the performance of the turbine (Nishi et al., 2014b). However, the flow fields in and around the blades were not fully measured because of challenges in optical access. Therefore,

the blade angle variations of the velocity field during the rotation of the turbine were not clarified. It is noteworthy that the effect of the free surface on the turbine performance is more complex in an open cross-flow hydraulic turbine than in a closed cross-flow turbine because the free surface is widely distributed over the blades of the open cross-flow turbine. Furthermore, Nishi et al. (2017) reported that open cross-flow hydraulic turbines performed better with fewer blades than closed-type turbines. Hence, the performances of the open and closed cross-flow hydraulic turbines differed significantly.

In this study, experimental and numerical studies of the flow around an open cross-flow hydraulic turbine in an underflow operation were conducted to analyze the torque mechanism of the turbine. The unsteady flow field in and around the turbine was measured via phase-averaged PIV, and the corresponding torque mechanism was investigated via two-dimensional numerical simulation based on the VOF method. The effects of the bottom spacing below the turbine and the channel wall in improving the performance of the open cross-flow hydraulic turbine were considered.

2.2 Experiments

Experiments were performed in an open-circuit water tunnel with a square cross-sectional area of 150 mm × 150 mm in the test section and a length of 400 mm, as described by Fujisawa and Takeuchi (1999). It is noteworthy that the working fluid water exited to the open tank downstream of the test section, thereby resulting in an atmospheric pressure at the water surface. The open cross-flow hydraulic turbine was located at the test section, with its center situated 85 mm from the bottom wall of the tunnel. The turbine was made of transparent acrylic resin for flow visualization purposes. The geometry of the open cross-flow hydraulic turbine is shown in Fig. 2-1. The turbine had an outer diameter D_o = 115 mm, an inner diameter D_i = 78 mm, a chord

length C = 20 mm, a width W = 146 mm, and N = 16 for the number of blades. The radius of the turbine was defined as R (= D_o/2) = 57.5 mm, and the thickness of the turbine blade was 2 mm with a rounded edge. The turbine was supported by two end walls of diameter 1.1D_o = 127 mm. The clearance between the turbine end wall and the channel side wall was set to 2 mm, which was sufficiently small to maintain the two-dimensional flow through the turbine. The number of blades used for the cross-flow hydraulic turbines was large enough to ensure efficiency (Nishi et al. 2017) as well as to facilitate the observation of the flow field through the blade passage. Each blade was made of a circular arc with inlet and outlet angles of 28° and 90°, respectively. In the present experiment, the upstream water level was maintained at H_u = 65 mm from the bottom wall of the channel. The distance between the bottom of the turbine and the channel wall was set to H_b/R = 0.48, (H_b = 27.5 mm) for a large bottom spacing and H_b/R = 0.30 (H_b = 17.5 mm) for a small bottom spacing, as examples of bottom spacing. The small bottom spacing was realized by inserting a 10-mm-thick plate of 340 mm long on the channel wall. The plate was tapered at the leading edge to remove flow separation. The geometrical scales and experimental conditions of the cross-flow hydraulic turbine are listed in Table 2-1. It is noteworthy that a smaller spacing may increase the three-dimensional flow near the end plates of the turbine.

The flow field in and around the open cross-flow hydraulic turbine was measured using a phase-averaged PIV system, which comprised a CW Nd:YAG laser, high-speed camera, and pulse generator (Fujisawa 1996; Fujisawa and Takeda 2004). The turbine was driven by a stepping motor that was rotatable by 0.5° using a pulse input. The PIV images were captured using a high-speed camera operating at a spatial resolution of 1280 × 1024 pixels and a frame rate of 500 fps. The target image size was 160 mm × 128 mm, which encompassed the flow in and below the turbine. Light sheet illumination was provided at the central section of the turbine using a CW Nd:YAG laser at 8 W power with a light sheet thickness of 2 mm. The mean velocity

in the test section was set to 0.2 m/s using an inverter by controlling the pump revolution, where the mean velocity was measured via PIV. Flow visualization was performed using nylon tracer particles measuring 80 μm in diameter, which appeared as particles measuring 3 pixels in diameter in the flow visualization images.

The PIV analysis of the flow in and around the cross-flow turbine was performed using direct cross-correlation analysis combined with the Gaussian subpixel interpolation technique (Kiuchi et al. 2005), where the correlation window size was set to 31 × 31 pixels. In the present experiment, the phase-averaged PIV technique was used to measure the velocity field, where the turbine was driven by a stepping motor with a pulse controller. The time-averaged flow field was obtained for every fixed blade angle of the cross-flow turbine. This experimental technique minimizes the experimental uncertainty in the measurement of the mean velocity fields. The statistical properties of the mean and fluctuating velocities were evaluated from 500 instantaneous velocity fields measured at fixed blade angles with a time interval of 2 ms. The maximum pixel displacement of the particle images was approximately 4 pixels; the invalid velocity vectors constituted less than 1% of the total number of velocity vectors analyzed. The uncertainty of the velocity measurement was estimated to be 3% at a 95% confidence level, with the major uncertainty arising from the effect of the out-of-plane velocity (Wieneke, 2015; Ikarashi et al., 2018).

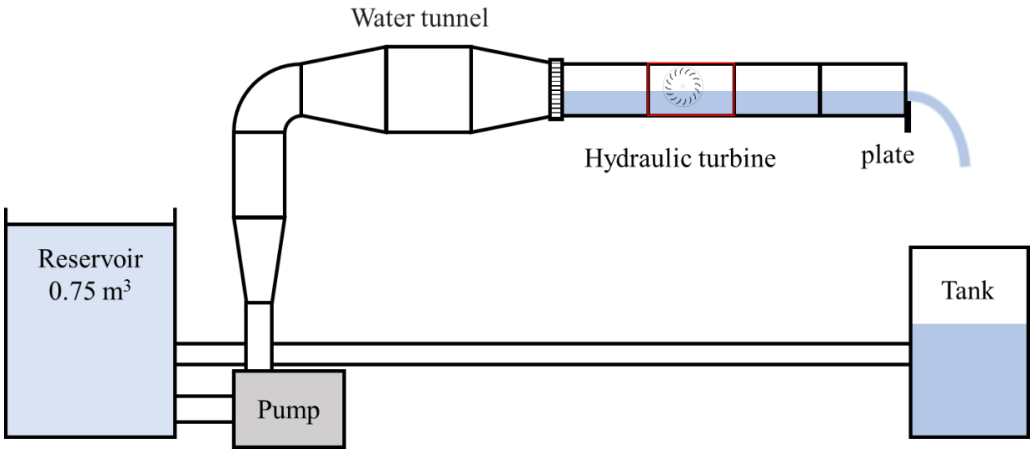

(a) Experimental setup

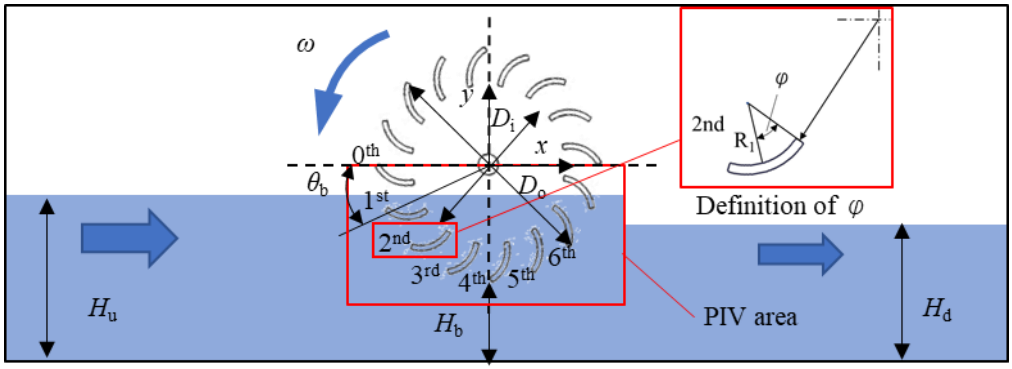

(b) Geometry of cross-flow hydraulic turbine

Fig.2-1 Experimental setup for open cross-flow hydraulic turbine

Table 2-1 Dimensions of open cross-flow hydraulic turbine

Outer diameter: D_o (mm)	115
Inner diameter: D_i (mm)	78
Radius of turbine: R (mm)	57.5
Radius of blade: R_1 (mm)	16.5
Inlet angle: β_i (°)	28
Outlet angle: β_o (°)	90
Rotor width: W (mm)	146
Chord length: C (mm)	20
Bottom spacing: H_b(mm)	27.5, 17.5
Number of blades: N	16

2.3 Numerical Methods

The numerical simulation of the flow field around a cross-flow hydraulic turbine was performed by solving the Reynolds-averaged Navier–Stokes equations and continuity equation combined with the VOF method, which allowed the two-phase flow computations of water and air in and around the turbine (Trivedi et al., 2013; Nishi et al., 2014a, 2014b).

$$\frac{\partial \rho U_i}{\partial t} + U_j \frac{\partial \rho U_i}{\partial x_j} = -\frac{\partial P}{\partial x_i} + \frac{\partial}{\partial x_j}\left(\mu \frac{\partial U_i}{\partial x_j} - \rho \overline{U_i' U_j'}\right) + \Delta \rho g + f_{\sigma i} \tag{2-1}$$

$$\frac{\partial U_j}{\partial x_j} = 0 \tag{2-2}$$

The third term on the right-hand side of Eq. (2-1) represents the buoyancy force and the last term is the surface tension effect taking into account the two-phase flow. The Reynolds-stress term is modeled by a gradient-type diffusion of the standard k–ε turbulence model:

$$\frac{\partial k}{\partial t}+U_{\mathrm{j}}\frac{\partial k}{\partial x_{\mathrm{j}}} = -\overline{U_{\mathrm{i}}^{'}U_{\mathrm{j}}^{'}}\frac{\partial U_{\mathrm{j}}}{\partial x_{\mathrm{j}}}+\frac{\partial}{\partial x_{\mathrm{j}}}\left\{\left(\nu+\frac{\nu_t}{\sigma_k}\right)\frac{\partial k}{\partial x_{\mathrm{j}}}\right\}-\varepsilon \tag{2-3}$$

$$\frac{\partial \varepsilon}{\partial t}+U_{\mathrm{j}}\frac{\partial \varepsilon}{\partial x_{\mathrm{j}}} = -C_{\varepsilon 1}\frac{\varepsilon}{k}\overline{U_{\mathrm{i}}^{'}U_{\mathrm{j}}^{'}}\frac{\partial U_{\mathrm{j}}}{\partial x_{\mathrm{j}}}+\frac{\partial}{\partial x_{\mathrm{j}}}\left\{\left(\nu+\frac{\nu_t}{\sigma_\varepsilon}\right)\frac{\partial \varepsilon}{\partial x_{\mathrm{j}}}\right\}-C_{\varepsilon 2}\frac{\varepsilon^2}{k} \tag{2-4}$$

$$-\overline{U_{\mathrm{i}}^{'}U_{\mathrm{j}}^{'}} = \nu_t\left(\frac{\partial U_{\mathrm{i}}}{\partial x_{\mathrm{j}}}+\frac{\partial U_{\mathrm{j}}}{\partial x_{\mathrm{i}}}\right)-\frac{2}{3}k\delta_{\mathrm{ij}}\ ,\ \nu_t=\frac{C_\mu k^2}{\varepsilon} \tag{2-5}$$

where δ represents the Kronecker delta, and empirical constants are given as follows: $\sigma_{\mathrm{k}} = 1.0$, $\sigma_\varepsilon = 1.3$, $C_{\varepsilon 1} = 1.44$, $C_{\varepsilon 2} = 1.92$, $C_\mu = 0.09$.

The governing equations were discretized using the finite volume method with a second-order upwind scheme. The pressure–velocity calculations for these equations were performed using the pressure-implicit with splitting of operator (PISO) algorithm (Issa, 1986) to reduce the computational cost in obtaining the convergence of calculations. The computations were performed using OpenFOAM 4.1 software.

In this study, two-dimensional unsteady flow analysis was introduced into the flow simulation because the target flow field in and around the cross-flow turbine was almost a two-dimensional two-phase flow, except for the flow near the end plates. Figure 2-2(a) shows the computational domain and geometry of the computational mesh, which consists of hexahedral element meshes in the computational domain. A uniform horizontal velocity was applied in the water-phase inlet boundary at $x/D_{\mathrm{o}} = -5$. The free-stream condition was applied to the velocity and static pressure at the downstream boundary at $x/D_{\mathrm{o}} = 13$. The wall function was applied on

the blade and bottom wall based on the assumption of a smooth wall surface, whereas the boundary condition at the top surface was switched between a free-stream outflow and a constant inflow to allow flow reversal (Trivedi et al., 2013). It should be mentioned that the water level at the upstream of turbine (x/D_o = - 2) was adjusted by try and error method to meet with the experimental water level 65mm by tuning the uniform inlet velocity and the water level under the condition of fixed flow rate. This is because the minor difference in the water level occurred immediate downstream of the inlet boundary once the transient start-up period was concluded. Figure 2-2(b) shows a magnified image of the mesh near the turbine. To rotate the blades at a given tip-speed ratio, an arbitrary mesh interface (AMI) boundary was introduced around the turbine, which was located at the radial distance of 59.5mm from the turbine center. Note that the time increment was set to 5×10^{-6} s in the numerical simulation, which corresponds to 0.001° of the turbine rotation at tip-speed ratio λ = 1.0. This boundary enabled the simulation across the disconnected and adjacent mesh domains. Therefore, the mesh in the domain rotated with the turbine. Since the simulation showed a transient state in the initial few rotations of the turbine dependent on the tip-speed ratio, the phase-averaged velocity and torque of the turbine were calculated from the data averaged over 20 cycles of periods once the transient start-up period was concluded. Grid convergence studies were performed with meshes comprising 80,000 (coarse), 110,000 (medium), and 150,000 (fine) cells. The relative errors of the coarse and medium meshes were 13% and 4%, respectively, with respect to the fine-mesh result of the average torque. A medium mesh was used for the parameter study as it afforded decent accuracy and incurred a reasonable computational cost. The minimum cell size was 0.1 mm in the medium mesh.

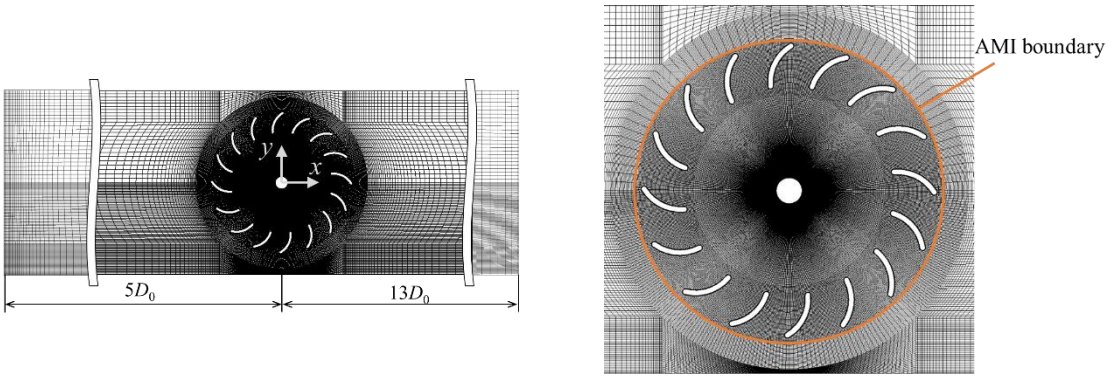

(a) Computational mesh (b) Enlarged mesh image near turbine

Fig. 2-2 Details of computational meshes

2.4 Results and Discussion

Table 2-2 summarizes the experimental and numerical results of the cross-flow turbine considered in this section, i.e., the tip-speed ratio λ (= $R\omega/U_0$), where R is the radius of the turbine, U_0 the free-stream velocity, and ω the angular velocity; bottom spacing H_b; upstream and downstream water levels H_u (at x/D_o = - 2) and H_d (at x/D_o = 2), respectively; water head H; as well as the torque coefficient C_t and power efficiency η obtained from numerical simulations. It is noted that the free-stream velocity of water flow U_0 = 0.2 m/s and the angular velocity of turbine ω = 1.74(rad/s) and 3.48(rad/s) for λ = 0.5 and 1.0, respectively.

Table 2-2 Summary of experimental and numerical results

λ	H_b (mm)	Experiment	Numerical simulation				
		H_u (mm)	H_u (mm)	H_d (mm)	H (mm)	C_t	η
0.5	27.5	65	65	60.1	4.4	0.627	0.242
	17.5		65	57.8	6.0	0.995	0.274
1.0	27.5		65	62.2	2.5	0.180	0.232
	17.5		65	60.2	4.0	0.387	0.309

2.4.1 Phase-averaged PIV measurements of velocity fields

Figures 2-3 and 2-4 show the phase-averaged velocity vectors of the open cross-flow hydraulic turbine for bottom spacing H_b/R of 0.48 and 0.30, respectively, with the tip-speed ratio set to λ= 0.5. The velocity magnitude U_m/U_0 is shown by color bars, where U_m ($=\sqrt{U^2+V^2}$), and U and V are the mean velocities in the x- and y-directions, respectively. Each figure shows a comparison of the experimental and numerical velocity fields at a fixed blade position with the tip of the zeroth blade (θ_b = 0°) set at the center of the cross-flow turbine (see Fig.2-1). The velocity fields are shown for the horizontal distance of x/R = -1.1 to 1.1 and vertical distance of y/R = -1.2 to 0 to encompass the entire flow field of the turbine of interest.

The measured velocity field (a) and numerical result (b) of the cross-flow hydraulic turbine agreed well with each other, except for the flow feature near the free surface. The main features of the flow field in and around the cross-flow hydraulic turbine, including the special features of accelerated flow through the blade passage in the hydraulic turbine and the formation of accelerated flow below the hydraulic turbine at the bottom spacing, were accurately reproduced in the numerical simulation. Hence, the numerical simulation of the flow in a cross-flow hydraulic turbine was validated using experimental velocity fields. It is noteworthy that a slight difference was observed between the experimental and numerical velocity fields for the results near the free surface. This might be caused by random fluctuations in the free surface and resulted in a difference of accelerated flow through the blade passage.

The phase-averaged velocity fields of the cross-flow hydraulic turbine with an intermediate bottom spacing H_b/R = 0.48 (Fig.2-3) exhibited notable features of accelerated flow in and around the hydraulic turbine, similar to those observed in the flow over the sixth blade (θ_b = 135°) and through the bottom spacing under the hydraulic turbine. However, the magnitude of the accelerated flow through the bottom spacing was larger than that through the blade passage. The

velocity field indicated that the flow entered the hydraulic turbine through the first to the fourth blades (θ_b = 22.5°–90°), and left from the blade passage of the fourth to sixth blades (θ_b = 90°–135°) downstream, where the flow was accelerated by the stagnation pressure effect on the concave side of the blade. The high-velocity flow prevailed at the convex side of the blade, where cavitation inception can be expected because of the formation of a low-pressure region (Adhikari et al., 2016). This accelerated flow exited to the flow below the hydraulic turbine, and a highly accelerated flow was formed through the bottom spacing; subsequently, it was combined with the converging flow effect of the flow between the hydraulic turbine and channel wall. The high-velocity region through the bottom spacing appeared periodically owing to the periodic shedding of the flow through the blade passages by the blade rotation.

When the bottom spacing below the hydraulic turbine was decreased to H_b/R = 0.30, (Fig.2-4), the features of the flow in and below the hydraulic turbine were magnified. Hence, the accelerated flow appeared in the flow around the fourth to sixth blades (θ_b = 90°–135°); the flow magnitude through the small bottom spacing increased significantly, whereas the remainder of the flow field exhibited a behavior similar to that observed for the large bottom spacing. The flow acceleration effect in the flow field might improve the performance of the hydraulic turbine.

Figures 2-5 and 2-6 show the phase-averaged velocity field of the open cross-flow hydraulic turbine with bottom spacing of H_b/R = 0.48 and 0.30, respectively, at a tip-speed ratio λ = 1.0. Each figure shows a comparison of the experimental and numerical velocity fields at a fixed blade angle. The results shown indicate that the accelerated flow appeared in the first to fourth blades (θ_b = 22.5°–90°), whereas that in the fourth to sixth blades (θ_b = 90°–135°) weakened. Therefore, the accelerated flow region in the hydraulic turbine shifted upstream with increasing tip-speed ratio from λ = 0.5 to 1.0. This result indicates that the accelerated flow in and below the hydraulic turbine was affected by the tip-speed ratio. Furthermore, the velocity field in and

around the hydraulic turbine with a small bottom spacing (Fig.2-6) exhibited an increased velocity in and below the hydraulic turbine owing to the converging flow effect in and through the bottom spacing. This is similar to the accelerated flow observed at the low tip-speed ratio of λ = 0.5, as shown in Figs. 2-3 and 2-4. The accelerated flow on the fourth to sixth blades (θ_b = 90°–135°) can still be observed because of the stagnation effect on the concave side of the blade as well as the high-velocity flow that formed on the convex side of the blade. It is noteworthy that a slight deviation in the velocity field was magnified in the blade passage downstream as the tip-speed ratio increased and the bottom spacing decreased, where the accelerated flow at the sixth blade (θ_b =135°) appeared at a smaller blade angle (θ_b =112.5°– 135°). These results show that the bottom spacing is an influential parameter that accelerates the flow in and below the open cross-flow hydraulic turbine, which may improve the turbine performance.

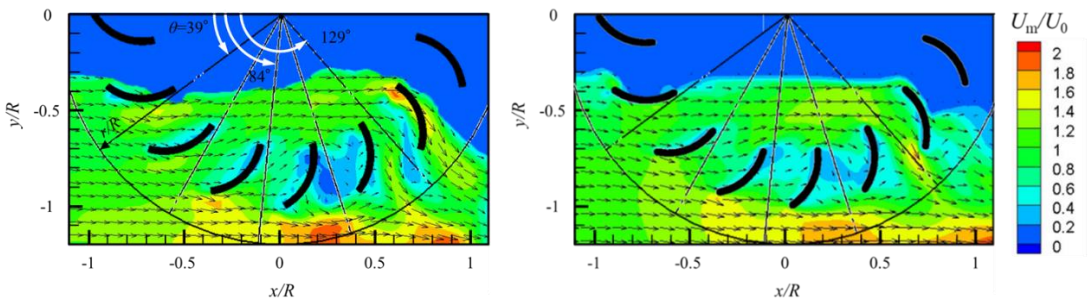

(a) Experimental flow field (b) Numerical flow field

Fig.2-3 Phase-averaged mean velocity field in open cross-flow hydraulic turbine at λ = 0.5 (H_b/R = 0.48).

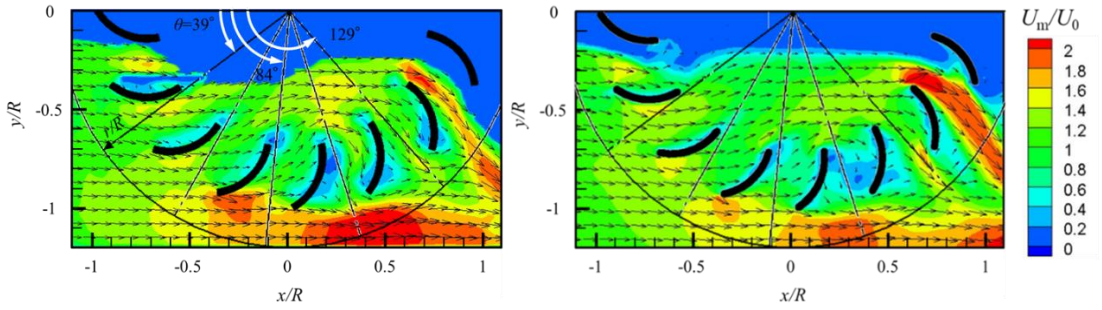

(b) Experimental flow field (b) Numerical flow field

Fig. 2-4 Phase-averaged mean velocity field of open cross-flow hydraulic turbine at $\lambda = 0.5$ ($H_b/R = 0.30$).

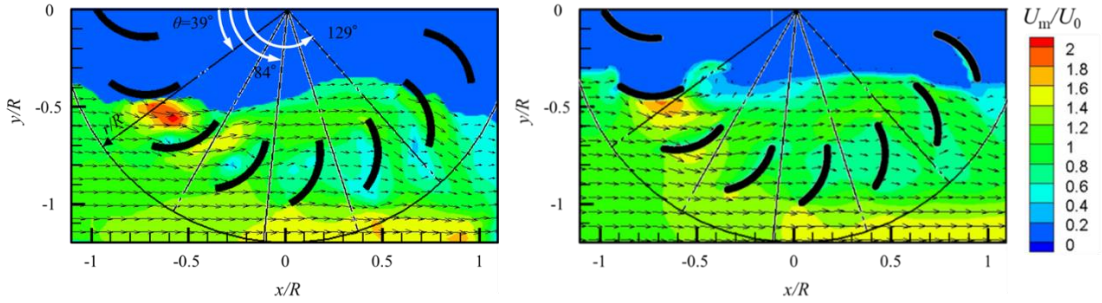

(a) Experimental flow field (b) Numerical flow field

Fig. 2-5 Phase-averaged mean velocity field in open cross-flow hydraulic turbine at $\lambda = 1.0$ ($H_b/R = 0.48$).

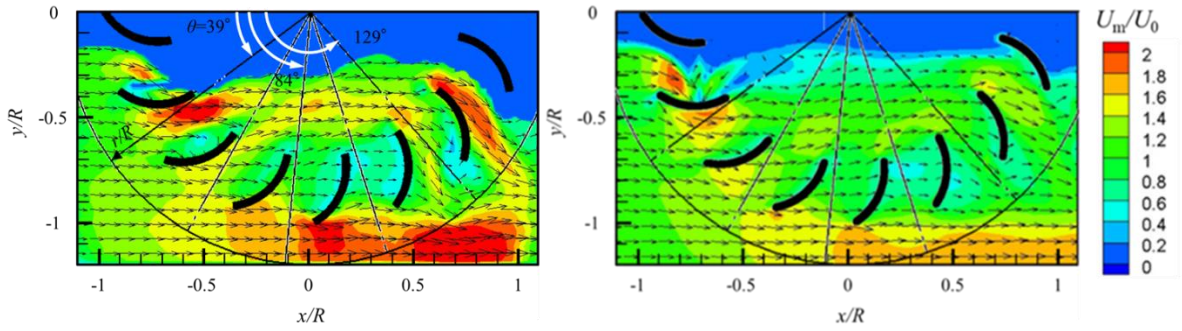

(a) Experimental flow field (b) Numerical flow field

Fig. 2-6 Phase-averaged mean velocity field of open cross-flow hydraulic turbine at $\lambda = 1.0$ ($H_b/R = 0.30$).

Figures 2-7 and 2-8 show the experimental and numerical results of cross-sectional phase-averaged velocity profiles in the cross-flow hydraulic turbine, in which results obtained with different bottom spacing of $H_b/R = 0.48$ and 0.30 at $\lambda = 0.5$ were compared. The results are shown for several angles, i.e.,. $\theta = 39°$ (between the first and second blades), 61.5° (between the second and third blades), 84° (between the third and fourth blades), 106.5° (between the fourth and fifth blades), and 129° (between the fifth and sixth blades) in and around the hydraulic turbine, as illustrated in Figs.2–3~2-6. These results indicate that the experimental velocity distributions through the blade passages were accurately reproduced in the numerical results, suggesting the validity of the numerical simulation. It is noteworthy that the ordinate r/R in Figs. 2-7 and 2-8 is the radial distance measured from the center of the hydraulic turbine down to the channel wall, as illustrated in Figs. 2–3~2-6, and that the blade passage is located at $r/R = 0.7$–1.0. A detailed analysis of the velocity field shows that the flow velocity in and around the hydraulic turbine increased in the small bottom spacing owing to the flow converging effect of the bottom spacing.

Figures 2-9 and 2-10 show the experimental and numerical results of the cross-sectional mean velocity profiles with bottom spacing H_b/R = 0.48 and 0.30, respectively, at λ = 1.0, which is a typical tip-speed ratio at a higher rotational speed of the turbine. These results indicate that a higher velocity appeared in and out of the turbine with a small bottom spacing, similar to the results shown in Figs. 2-7 and 2-8 at a small tip-speed ratio λ = 0.5. Therefore, the overall velocity in the turbine increased at the small bottom spacing, independent of the tip-speed ratio. The small bottom spacing affected not only the flow through the bottom spacing, but also the flow field in the turbine. The velocity distribution in the turbine became more uniform at higher tip-speed ratios owing to the more prominent blade rotation effect. It is noteworthy that the wake effect of the blade in the velocity distribution (θ = 61.5°~106.5°) was removed at an angle θ =129°, owing to the flow through the blade passage to the outside of the turbine. These results indicate that the velocity distribution in and around the open cross-flow hydraulic turbine was reproduced well by the numerical simulation, whereas the velocity field near the free surface deviated from the measurements at increased tip-speed ratio. This might be due to three-dimensional effect of free surface in the experiment, and shows the limitation of two-dimensional flow computation.

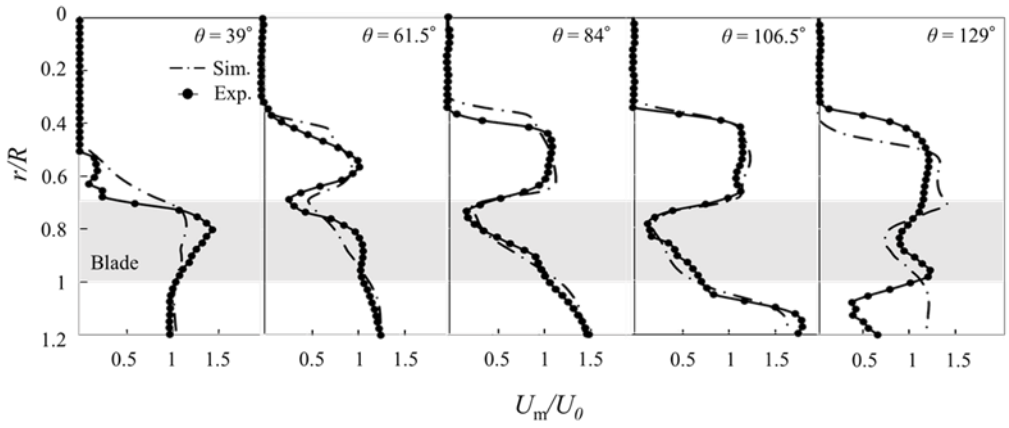

Fig. 2-7 Cross-sectional mean velocity profiles U_m/U_0 in cross-flow hydraulic turbine at λ = 0.5 (H_b/R = 0.48).

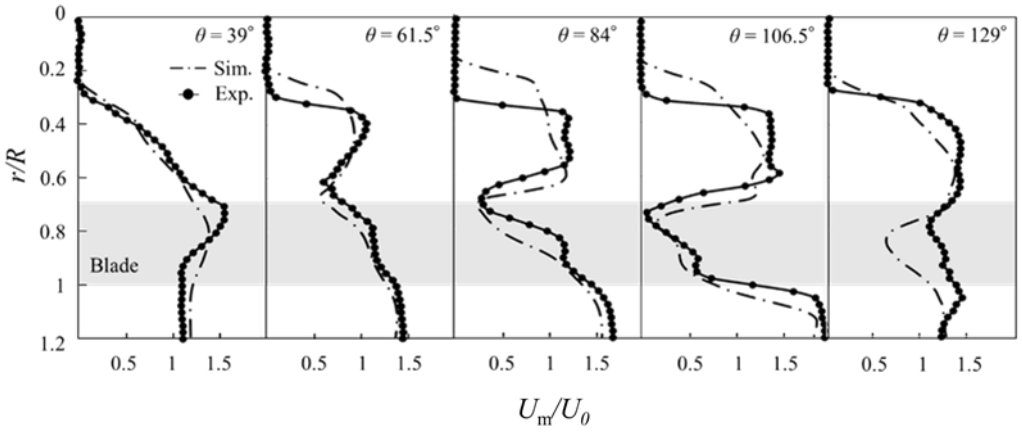

Fig.2-8 Cross-sectional mean velocity profiles U_m/U_0 in cross-flow hydraulic turbine at $\lambda = 0.5$ ($H_b/R = 0.30$).

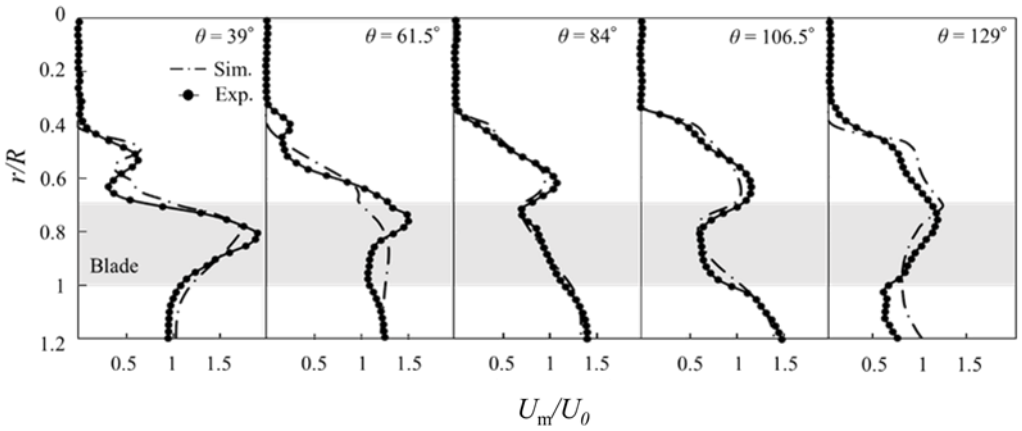

Fig. 2-9 Cross-sectional mean velocity profiles U_m/U_0 in cross-flow hydraulic turbine at $\lambda = 1.0$ ($H_b/R = 0.48$).

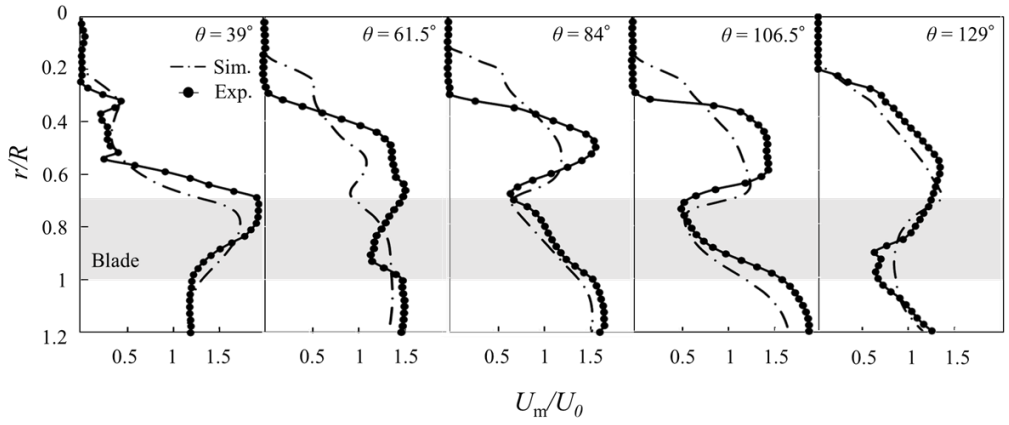

Fig. 2-10 Cross-sectional mean velocity profiles U_m/U_0 in cross-flow hydraulic turbine at $\lambda = 1.0$ ($H_b/R = 0.30$).

2.4.2 Local torque distribution on rotating blades

Figure 2-11 shows the numerical results of the local torque coefficient distributions imposed on the rotating blades of the cross-flow hydraulic turbine with different bottom spacing (U_m/U_0 = 0.48, and 0.30) at $\lambda = 0.5$. The local torque coefficient $C_{t\theta}$' is defined as follows:

$$C_{t\theta}' = \frac{2R_1 r}{D_o^2} \Delta C_p \cdot \cos\varphi \tag{2-6}$$

where

$$\Delta C_p = \frac{p_1 - p_2}{\frac{1}{2}\rho U_0^2} \tag{2-7}$$

where p_1 and p_2 are the pressures on the concave and convex sides, respectively; D_o is the outer diameter of the turbine; r is the radial distance from the center of the hydraulic turbine; R_1 is the blade radius; φ is the angle on each blade defined in Fig. 2-1 (Fujisawa and Gotoh, 1994). The results with large bottom spacing H_b/R = 0.48 indicated that the local torque coefficient $C_{t\theta}$' increased with the blade angle θ_b up to 112.5°. The maximum torque was observed at θ_b =112.5°, where the accelerated flow occurred on the fifth blade owing to the blade rotation effect, as observed in Figs. 2-3 and 2-7. A detailed analysis of the local torque distributions at H_b/R = 0.48

showed a slightly negative local torque at θ_b = 22.5°; however, the negative local torque coefficient decreased when the blade angle increased to θ_b = 45°. With a further increase in the blade angle, the local torque coefficient became positive and increased up to θ_b = 112.5°. This local torque variation with the blade angle was consistent with the formation of accelerated flow through the blade passages at large blade angles. Hence, the local torque mechanism was closely associated with the formation of an accelerated flow at large blade angles.

A comparative study of the local torque coefficient distributions with a small bottom spacing H_b/R = 0.30 indicated an increased local torque at θ_b = 135° caused by the stagnation pressure imposed on the concave side of the blade and the formation of a high-velocity flow on the convex side of the blade. However, the remainder of the local torque distribution indicated slight changes at small blade angles. A detailed analysis of the local torque coefficient indicated that at θ_b = 22.5°, the negative torque increased slightly on the outer side of the blade, but it highly decreased on the inner side. The positive torque increased when the blade angle increased from θ_b = 45° to 112.5°, similar to the result of the large bottom spacing (H_b/R = 0.48), whereas the positive torque increased abruptly at θ_b = 135° with a small bottom spacing, i.e., greater than the result of the large bottom spacing. These results indicate that the local torque on the blade increased with a small bottom spacing at large blade angles. The negative torque at the small blade angle was caused by the flow over the convex side of the blade, serving as the torque in the reverse direction.

Figure 2-12 shows the local torque coefficient distributions on the blade of the cross-flow hydraulic turbine with different bottom spacings (H_b/R = 0.48, 0.30) at λ = 1.0. The blade angle variation in the local torque distribution indicated a behavior similar to the case of the low tip-speed ratio λ = 0.5, as shown in Fig. 2-11; however, a slight difference was observed at small and large blade angles. The negative torque increased at a small blade angle θ_b = 22.5° at λ = 1.0,

and the positive torque decreased at a large blade angle θ_b = 135° in comparison with λ = 0.5. Furthermore, the local torque variation with the bottom spacings is decreased at λ = 1.0. Therefore, the improved torque performance of the cross-flow hydraulic turbine with a small bottom spacing is deteriorated at higher tip-speed ratio. It appeared that the negative local torque increased with the tip-speed ratio, owing to the local negative torque generated by the higher velocity of the blade at a large tip-speed ratio.

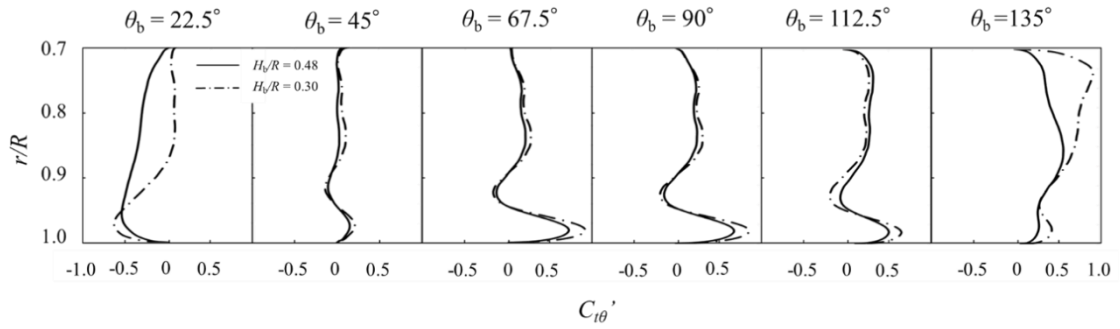

Fig. 2-11 Local torque coefficient $C_{t\theta}$' distributions on blades of open cross-flow hydraulic turbine at λ = 0.5 (H_b/R = 0.48, 0.30).

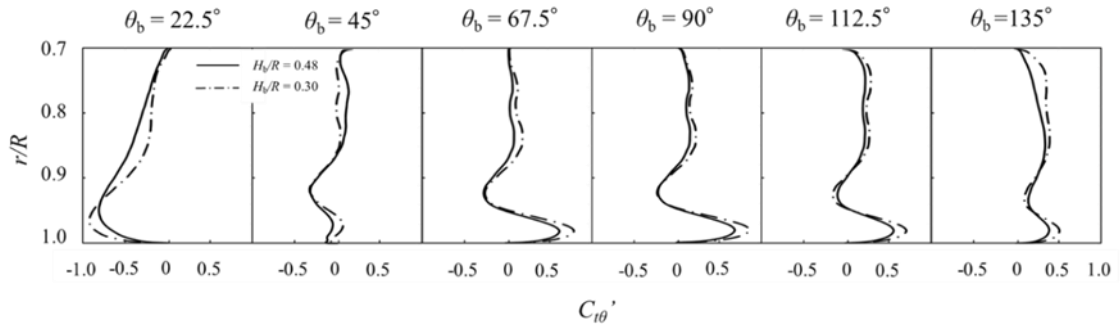

Fig. 2-12 Local torque coefficient $C_{t\theta}$' distributions on blades of open cross-flow hydraulic turbine at λ = 1.0 (H_b/R = 0.48, 0.30).

2.4.3 Torque mechanism of cross-flow turbine

Figures 2-13 and 2-14 show the numerical results of the blade-averaged torque coefficient $C_{t\theta}$ at tip-speed ratios λ = 0.5 and 1.0, respectively, which were plotted against the blade angle θ_b. The results of the cross-flow hydraulic turbine at λ = 0.5 (Fig. 2-13) show that the blade-averaged torque coefficient becomes negative at small blade angle θ_b = 22.5°, but it increases to the highest positive torque at large blade angle θ_b = 135°. This corresponds to the stagnation pressure effect on the convex side of the blade at small blade angle, and that on the concave side combined with the formation of high-velocity region in and around the turbine at large blade angle, respectively, as shown in Fig. 2-3. On the other hand, the negative torque decreased at small blade angles of a small bottom spacing, and the positive torque increased at large blade angle θ_b = 135° of the small bottom spacing, resulting in an increased mean torque coefficient of the cross-flow turbine. Therefore, the torque coefficient of the open cross-flow turbine can be increased at a small bottom spacing. It is noteworthy that the increased mean torque of the cross-flow turbine might be caused by the increased accelerated flow through the small bottom spacing, as shown in the mean velocity distributions in Figs.2-3 and 2-4.

When the tip-speed ratio increased to λ = 1.0, the blade-averaged torque coefficient varied with the blade angle, as shown in Fig. 2-14. The maximum and minimum torque coefficients were observed at θ_b = 135° and 22.5°, respectively. Hence, the torque variation with the blade angle occurred similarly to that observed at λ = 0.5; however, the positive torque decreased and the negative torque increased as the tip-speed ratio increased. Therefore, the torque performance of the open cross-flow hydraulic turbine deteriorated at a larger tip-speed ratio owing to the decreased relative flow velocity with respect to the blade rotation. Although the negative torque remains the same at small blade angles of small bottom spacing, the positive torque slightly increased at large blade angles, resulting in a slight increase in the positive torque with a small

bottom spacing. These results indicate that the torque performance of the cross-flow turbine can be improved by decreasing the bottom spacing, but the effect of the bottom spacing appeared to be saturated at large tip-speed ratios. The decrease in torque with increasing tip-speed ratio appeared similarly to the accelerating-flow behavior in the bottom spacing, as shown in Figs. 2-3~2-6. Hence, the blade-averaged torque performance was correlated significantly with the flow-field variation in the open cross-flow hydraulic turbine.

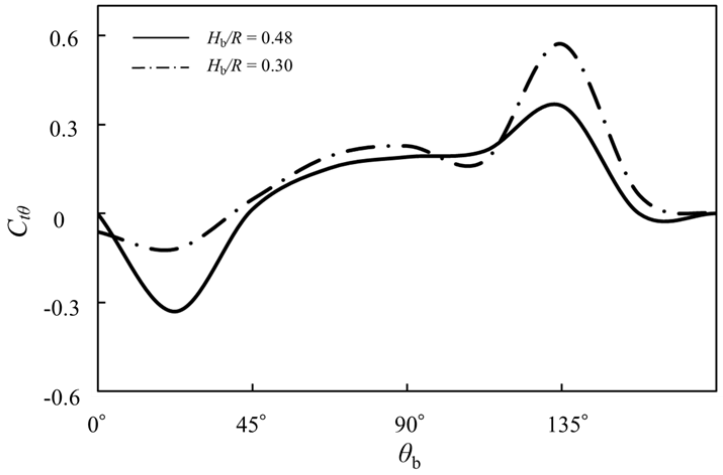

Fig. 2-13 Variation in blade-averaged torque coefficient $C_{t\theta}$ with blade angle θ_b at $\lambda = 0.5$.

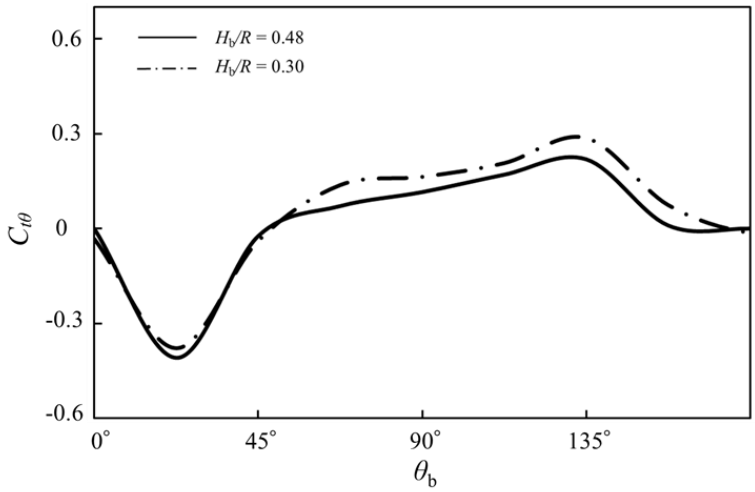

Fig. 2-14 Variation in blade-averaged torque coefficient $C_{t\theta}$ with blade angle θ_b at $\lambda = 1.0$.

Figures 2-15 and 2-16 show the torque coefficient C_t and power efficiency η of the cross-flow hydraulic turbine, which were plotted against the tip-speed ratio λ, with C_t, η are defined as follows:

$$C_t = \frac{T}{\frac{1}{4}\rho U_0^{\ 2} D_o^{\ 2}} \tag{2-8}$$

$$\eta = \frac{T\omega}{\rho g Q H} \tag{2-9}$$

where Q is the water flow rate, and H is the water head defined by

$$H = H_u + \frac{U_0^{\ 2}}{2g} - H_d - \frac{U_d^{\ 2}}{2g} \tag{2-10}$$

where H_u is the upstream water head, H_d the downstream water head, U_0 the free-stream velocity, and U_d the downstream velocity. The results indicate that the torque coefficient C_t decreased as the tip-speed ratio λ increased; however, the efficiency η was the maximum at λ = 0.8–0.9, and it decreased with a further increase in the tip-speed ratio λ. The present result with a small bottom spacing indicates a higher maximum efficiency (η_{max} = 0.39 at H_b/R =0.30) than those with a large bottom spacing (η_{max} = 0.32, H_b/R = 0.48). This result indicates that the cross-flow hydraulic turbine performance can be improved by decreasing the bottom spacing between the turbine and channel wall. The experimental efficiency taken from Nishi et al. (2014a) is plotted in Fig.16 for comparison. This is a case of very small bottom spacing H_b/R = 0.06 and the peak efficiency is η_{max} = 0.23 at λ= 0.75. This result indicates that

the lower efficiency was obtained at very small bottom spacing. It is expected that the bottom spacing is an influential parameter and very small bottom spacing may not be effective for the efficiency of the cross-flow hydraulic turbine. This may be caused by the formation of three-dimensional flow toward the side wall of the turbine at very small bottom spacing, and it cannot be predicted by the two-dimensional numerical simulation. It is noteworthy that the efficiency of the cross-flow hydraulic turbine can be affected by the diameter ratio and number of blades. According to a previous study pertaining to the performances of closed hydraulic turbines, the efficiency increased slightly after optimizing the diameter ratios and number of blades (Sammartano, et al., 2015). Such optimizations are applicable for open cross-flow hydraulic turbines; the associated flow-field variations have not been analyzed previously and hence will be investigated in future studies.

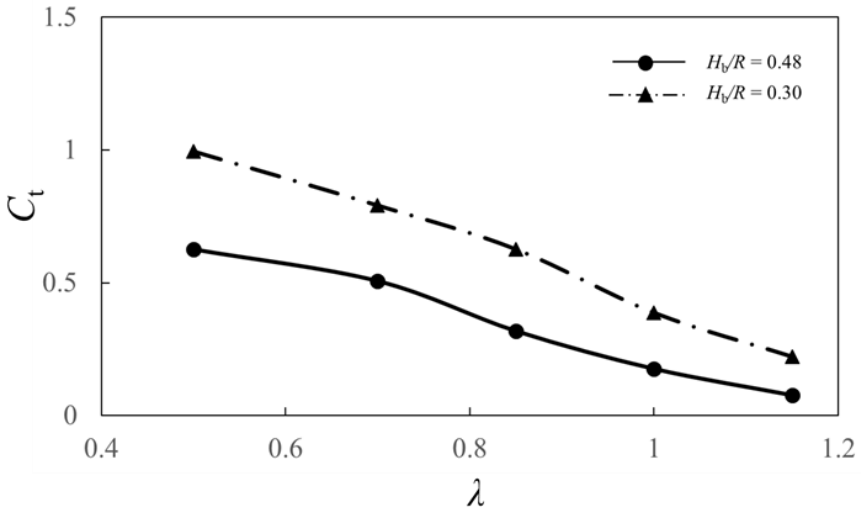

Fig. 2-15 Variation in torque coefficient C_t with tip-speed ratio λ.

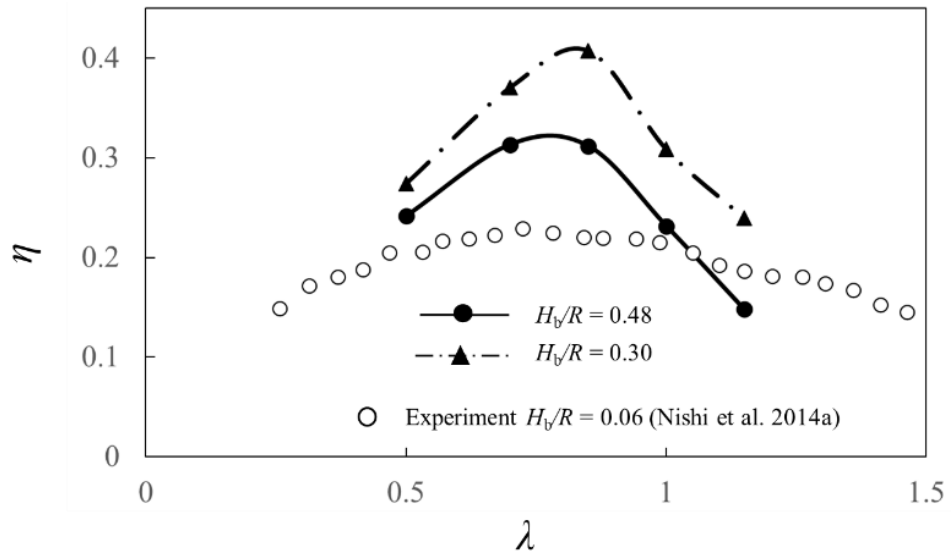

Fig. 2-16 Variation in efficiency η with tip-speed ratio λ.

2.5 Conclusions

The flow fields in and around an open cross-flow hydraulic turbine in an underflow operation were investigated via velocity measurements using PIV and two-dimensional numerical simulations based on the VOF method. The experimental and numerical results agreed reasonably well with each other, thereby suggesting the validity of the numerical results. The experimental and numerical results indicated that both the accelerated flow over the blade at large blade angles in the downstream and through the bottom spacing between the turbine and channel wall contributed to the positive torque generation in the open cross-flow hydraulic turbine. The former effect could be caused by the stagnation pressure effect on the concave side of the blade and the formation of a high-velocity flow on the convex side of the rotating blade appearing at a low tip-speed ratio. The latter effect of bottom spacing could be caused by the converging flow between the turbine and channel wall. These flow features improved when the bottom spacing was decreased, resulting in a local torque generation that might improve the torque and efficiency of the hydraulic turbine. However, the accelerated flow through the blade

passage at small blade angles increased with the tip-speed ratio and could result in a negative torque, resulting in a deteriorated torque performance at high tip-speed ratios. These results indicate that flow control by decreasing the bottom spacing of the turbine can be effective for improving the efficiency of open cross-flow hydraulic turbines in an underflow operation, owing to enhanced flow features in and around the open cross-flow turbine. However, very small bottom spacing may not be effective for improving the efficiency.

References

Fujisawa, N., & Gotoh, F. (1994) Experimental study on the aerodynamic performance of a Savonius rotor. ASME Journal of Solar Energy Engineering, 116, 148-152.

Fujisawa, N., & Takeuchi, M. (1999) Flow visualization and PIV measurement of flow field around a Darrieus rotor in dynamic stall. Journal of Visualization, 1, 379-386.

Fujisawa, N. (1996) Velocity measurements and numerical calculations of flow fields in and around Savonius rotors. Journal of Wind Engineering and Industrial Aerodynamics, 59, 39-50.

Fujisawa, N., Takeda G., & Ike, N. (2004) Phase-averaged characteristics of flow around a circular cylinder under acoustic excitation control. Journal of Fluids and Structures, 18, 159-170.

Ikeda, T., Iio, S. & Tatsuno, K. (2010) Performance of nano-hydraulic turbine utilizing waterfalls. Renewable Energy, 35, 293–300.

Ikarashi, Y., Uno, T., Yamagata, T., & Fujisawa, N. (2018) Influence of elbow curvature on flow and turbulence structure through a 90° elbow. Nuclear Engineering and Design, 339, 181-193.

Issa, R. I. (1986) Solution of the implicitly discretized fluid flow equations by operator-splitting. Journal of Computational Physics, 62, 40-65.

Kiuchi, M., Fujisawa, N., & Tomimatsu, S. (2005) Performance of PIV system for combusting flow and its application to spray combustor model. Journal of Visualization, 8, 269–276.

Nishi, Y., Inagaki, T., Li, Y., Omiya, R., & Fukutomi, J. (2014a) Study on an undershot cross-flow water turbine. Journal of Thermal Science, 23, 239-245.

Nishi, Y., Inagaki, T., Li, Y., Omiya, R., & Hatano, K. (2014b) The flow field of undershot cross-flow water turbines based on PIV measurements and numerical analysis. International Journal of Fluid Machinery System, 7, 174-182.

Nishi, Y., Hatano, K., & Inagaki, T. (2017) Study on performance and flow field of an undershot cross-flow water turbine comprising different number of blades. Journal of Thermal Science, 26, 413–420.

Sammartano, V., Aricò, C., Sinagra, M., & Tucciarelli, T. (2015) Cross-flow turbine design for energy production and discharge regulation. Journal of Hydraulic Engineering, 141, doi :10. I 061 /(ASCE)HY. 1943 -7900.0000977.

Trivedi, C., Cervantes, M. J., Gandhi, B. K., Dahlhaug, O. G. (2013) Experimental and numerical studies for a high head Francis turbine at several operating points. ASME Journal of Fluids Engineering, 135, 111102 (17 pages).

Uchiyama, T., Uehara, S., Fukuhara, H., Iio, S., & Ikeda, T. (2015) Numerical study on the flow and performance of an open cross-flow mini-hydraulic turbine. Proceedings of the IMechE Part A, Journal of Power and Energy, 229, 968-977.

Chapter 3 Experimental and numerical studies on the performance of waterfall-type cross-flow hydraulic turbine

3.1 Introduction

When there is an enough water head, the open cross-flow hydraulic turbine can be operated in waterfall condition. Such hydraulic turbine operation is more suitable to power generation because the water flow can be easily controlled to gain higher efficiency of the turbine than that of the underflow operation. This could be caused by more efficient conversion of the water head into fluid kinetic energy because of the concentrated water flow on the advancing blade side of the turbine, which rotates in the same direction as the water flow.

Uchiyama et al. (2015) reported by experiment that the power efficiency of the waterfall-type cross-flow hydraulic turbine is approximately 53%, which is larger than that of the open cross-flow turbine in underflow operation. Moreover, the numerical simulation was carried out by particle methods to understand the flow mechanism and the performance of the waterfall-type cross-flow hydraulic turbine. Generally speaking, the numerical result rather well reproduces the experimental performance. However, the experimental result suffered from three-dimensional effects of the upstream flow arising from the long distance of the waterfall before approaching the turbine. Therefore, the assumption of two-dimensional flow in numerical

simulations may not be valid to compare with the experimental efficiency of waterfall-type cross-flow hydraulic turbines. To overcome this difficulty, there is a strong demand for experimental investigations of the power efficiency of two-dimensional waterfall-type cross-flow hydraulic turbines. Furthermore, the applicability of numerical simulation using the VOF method for two-phase flow analysis should be further investigated, because it is widely applied in predicting the performance of most cross-flow hydraulic turbines in the literature (Sammartono et al., 2013; Nishi et al., 2014a; Adhikari & Wood, 2018a; Wang et al., 2021).

The purpose of this study is to investigate the performance of a waterfall-type cross-flow hydraulic turbine both experimentally and numerically under the condition of a two-dimensional waterfall. To validate the numerical approach using the VOF method, a two-dimensional flow experiment was carried out by measuring the torque and efficiency of the turbine. Furthermore, measurements of the mean velocity field in and around the hydraulic turbine were performed using phase-averaged particle image velocimetry (PIV) to compare with the results of the numerical simulations. Then, the torque mechanism of the turbine considered is elucidated based on flow field measurements and numerical local torque distributions with respect to variations in angle of blade position.

3.2 Experimental methods

3.2.1 Experimental setup

The performance of the waterfall-type cross-flow hydraulic turbine was evaluated using the experimental setup shown in Fig.3-1, consisting of a horizontal water channel with a cross-sectional area of 150 mm × 150 mm, followed by a vertical two-dimensional converging nozzle with an exit 5.3 mm thick and 150 mm wide. Note that the nozzle width was slightly larger than the width of the turbine itself at W=146 mm, to cover the entire width. The depth of the water

channel was maintained at 56 mm during the experiment. The waterfall-type cross-flow hydraulic turbine was situated 110 mm downward from the nozzle exit with a certain horizontal offset distance L from the turbine center, as shown in Fig.3-1. The offset distance could be varied to change the impingement position of the waterfall on the advancing blades, which rotated in the same direction as the waterfall, as shown in Fig.3-1.

The waterfall-type cross-flow hydraulic turbine with circular arc blades in section was constructed using a transparent acrylic resin material of 2 mm thickness for flow visualization purposes. The dimensions of the hydraulic turbine were as follows. The outer diameter D_o=115 mm, the inner diameter D_i=78 mm, and the blade radius R_1=16.5 mm with inlet and outlet angles of 28 ° and 90°, respectively, which were the same as an underflow cross-flow hydraulic turbine reported in the literature (Wang et al., 2021). The dimensions and basic characteristics of the hydraulic turbine considered are listed in Tables 3-1 and 3-2, respectively. Note that the number of blades N=16 was large enough to ensure efficiency (Nishi et al. 2017) as well as to facilitate the observation of the flow field through the blade passage. The experiments were carried out at a constant volume flow rate Q =0.00153 m^3/s, which was measured by the bulk flow method.

3.2.2 Inlet velocity condition

The two-dimensional mean velocity distributions at the exit of the nozzle were measured by traversing a total pressure tube 1 mm in diameter in a spanwise direction along the center of the nozzle. The result is shown in Fig. 3-2, where the mean velocity U is rendered dimensionless by the bulk velocity U_e at the nozzle exit, and the result is plotted against the dimensionless spanwise distance z by the turbine width W (=146 mm). The mean velocity distribution of the waterfall downstream of the nozzle is almost uniform in the spanwise direction, suggesting a two-dimensional mean velocity distribution at the waterfall inlet.

3.2.3 Torque and power measurements

Torque measurements were carried out using an electric torque converter located between the hydraulic turbine and a connected stepper motor. The angular velocity of the hydraulic turbine was measured using a noncontact-type photosensor. It should be mentioned that the friction loss of the hydraulic turbine on the supporting bearing was confirmed to be small by measurement of the frictional torque of the turbine in air driven by the stepper motor. The frictional torque was considered an uncertainty of the torque measurement.

3.2.4 Phase-averaged PIV measurements

The velocity field of the waterfall-type cross-flow hydraulic turbine was measured by phase-averaged particle image velocimetry (PIV) without adding any tracer particles by illuminating the central cross-section of the hydraulic turbine normal to the flow axis. Light-sheet illumination was provided using a CW: Nd:YAG laser of 8W power with a 2 mm-thick laser. A total of 500 sets of instantaneous flow images were captured by a high-speed CMOS camera with a spatial resolution of 1024×1024 and a 12-bit depth in grayscale operating at 1000 frames per second. It should be noted that these PIV images at fixed angle of blade position were taken in reference to the angle signal from the stepper motor at every 22.5° with the tip of the top blade being set to the vertical ($\theta_b = 0°$) (Fujisawa, 1996; Fujisawa et al., 2004). These PIV images were analyzed by direct cross-correlation analysis using a sub-pixel interpolation technique (Kiuchi et al., 2005). It should be mentioned that the planar-image-pattern variation of the waterfall illuminated by the laser sheet was considered as the pattern displacement of waterfall images in the PIV analysis using an interrogation window size of 31×31 pixels (Fujisawa et al., 2012). Less than 2 % of the total number of analyzed velocity vectors were invalid, and the invalid vectors were replaced by an average of the neighboring 4 velocity vectors.

The maximum pixel displacement of the images was approximately 4 pixels, and the uncertainty of the measured velocity was approximately 3 % (Wieneke, 2015; Ikarashi et al., 2018). Examples of visualized images of the flow around the turbine are shown in Fig.3-3(a) and (b), which were taken at the spanwise center plane (z=0) while the cross-flow hydraulic turbine was operating at tip-speed ratio $\lambda(=R\omega/U_e)$ = 0.3 and 0.7, respectively, with the off-axis distance L=40mm, where R is the radius of the turbine. The visualized flow field images showed the splash pattern across the waterfall and indicated a major difference in the intensity of the advancing and returning blades, where the water flow exited the turbine. Moreover, the image pattern of the water flow on the turbine appeared to be affected by the tip-speed ratio. The flow image appeared in a wide angle of blade position at λ=0.3, while it was not fully observed at a large tip-speed ratio of λ=0.7. Thus, different flow behaviors were qualitatively observed on the visualized image patterns under the influence of varying tip-speed ratio. In contrast, the image pattern of the returning blades indicated inevitable droplet patterns on the end plate. These droplets are known to be caused by splashes and may have caused the invalid velocity vectors in the PIV analysis. It is noted that a circular black area appears near the center of the hydraulic turbine in the images presented, showing the supporting bearing of the axis (10 mm in diameter) of the turbine.

Table 3-1 Dimensions of cross-flow hydraulic turbine

Chord length: C (mm)	20
Outer diameter: D_o (mm)	115
Inner diameter: D_i (mm)	78
Diameter of endplate (mm)	127
Number of blades: N	16
Radius of turbine: R (mm)	57.5
Radius of blade: R_1 (mm)	16.5
Width of turbine: W (mm)	146
Blade angle: φ (°)	75
Inlet angle: β_i (°)	28
Outlet angle: β_o (°)	90

Table 3-2 Experimental conditions

Nozzle exit height He (m)	0.266
Flow rate Q (m^3/s)	0.00153
Inlet velocity (m/s)	1.93
Nozzle exit area (mm^2)	150 mm×5.3 mm

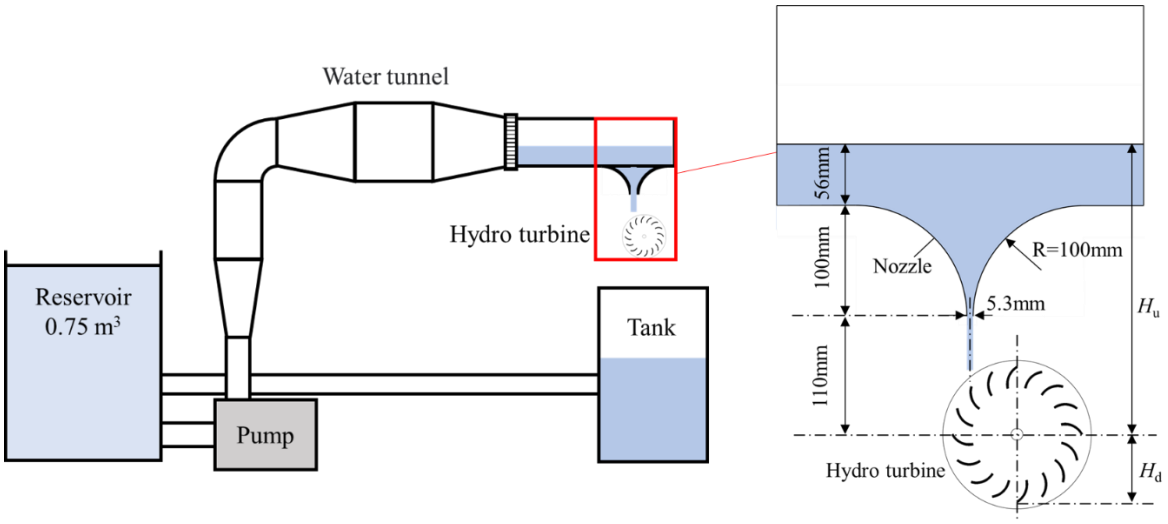

(a) Experimental setup (b) Enlarged view of nozzle flow

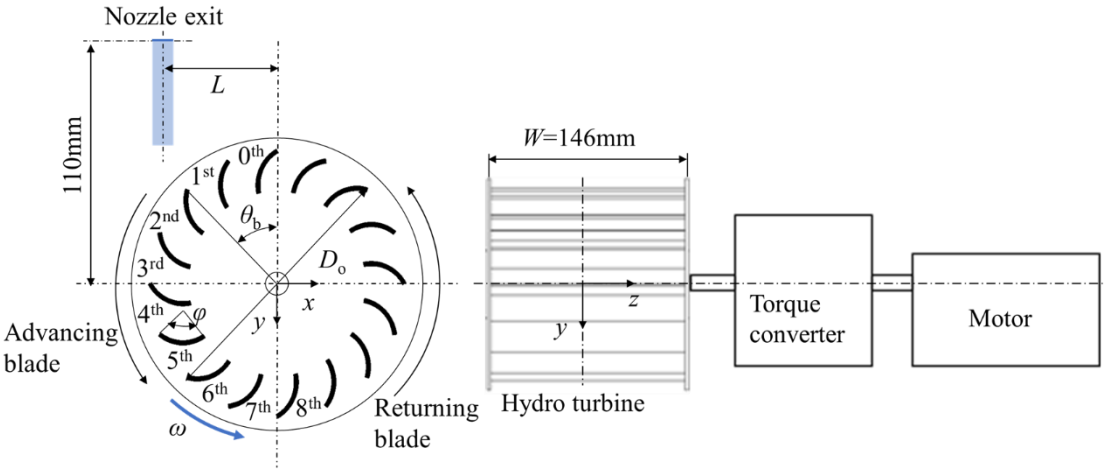

(c) Details of the cross-flow hydraulic turbine.

Fig.3-1 Experimental setup for waterfall-type cross-flow hydraulic turbine.

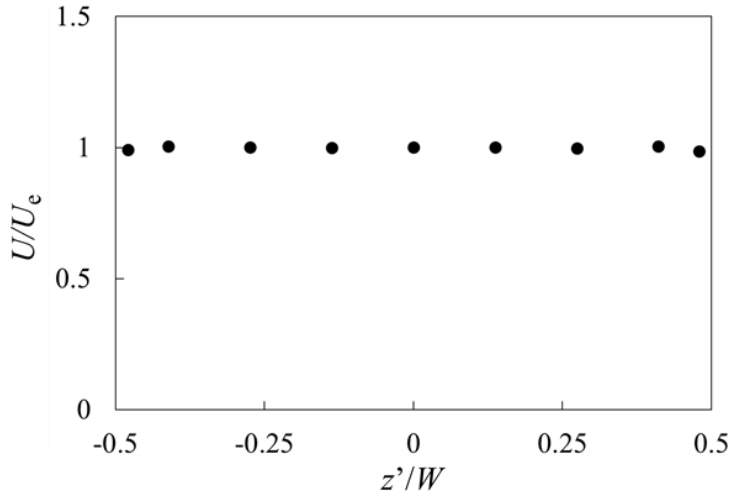

Fig.3-2 Spanwise mean velocity distribution of waterfall at nozzle exit (y = -110mm).

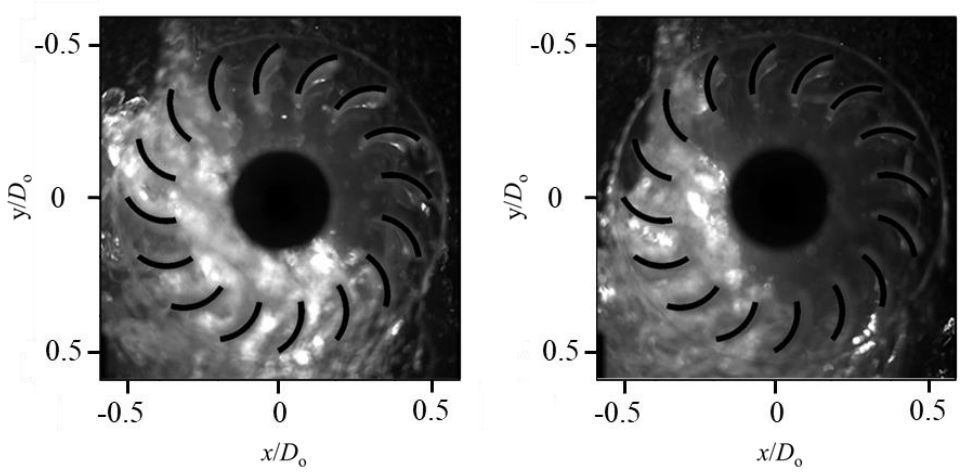

(a) λ = 0.3 (b) λ = 0.7

Fig.3-3 Flow visualization (L/D_o = 0.35).

3.3 Numerical Simulation

The performance of the hydraulic turbine was evaluated in a two-dimensional unsteady flow analysis using the Reynolds-averaged Navier-Stokes equations, continuity equation combined with the VOF method, which allowed the two-phase flow computations of water and air in and around the turbine (Trivedi et al., 2013; Nishi et al., 2014a, 2014b).

$$\frac{\partial \rho U_i}{\partial t} + U_j \frac{\partial \rho U_i}{\partial x_j} = -\frac{\partial P}{\partial x_i} + \frac{\partial}{\partial x_j}\left(\mu \frac{\partial U_i}{\partial x_j} - \rho \overline{U_i' U_j'}\right) + \Delta \rho g + f_{\sigma i} \tag{3-1}$$

$$\frac{\partial U_j}{\partial x_j} = 0 \tag{3-2}$$

The second term on the right-hand side of Eq. (3-1) represents the buoyancy force and the last term is the surface tension effect taking into account the two-phase flow. The Reynolds-stress term is modeled by a gradient-type diffusion of the standard k–ε turbulence model:

$$-\overline{U_i' U_j'} = \nu_t \left(\frac{\partial U_i}{\partial x_j} + \frac{\partial U_j}{\partial x_i}\right) - \frac{2}{3} k \delta_{ij} \ , \ \nu_t = \frac{C_\mu k^2}{\varepsilon} \tag{3-3}$$

where C_μ is an empirical constant given by 0.09, and δ represents the Kronecker delta.

The governing equations were discretized using the finite volume method with a second-order upwind scheme. The pressure–velocity calculations for these equations were performed using the pressure-implicit with splitting of operator (PISO) algorithm (Issa, 1986) to reduce the computational cost in obtaining the convergence of calculations. The computation was conducted using the OpenFOAM 4.1 software package. 120,000 total computational grids were used in this numerical simulation in reference to the numerical study at different number of grids. The computation at 90,000 grids agreed with this result within 0.2%, but it differed 4.6% with that at 70,000 grids.

The upstream boundary condition was set at the nozzle exit, which was y = -110 mm above the center of the hydraulic turbine. The uniform inlet velocity U_e (= 1.93 m/s) and total water head H_e (= 266 mm) were set at the nozzle exit with the full width of the nozzle (= 5.3 mm). The zero gradient condition was applied to the velocity and total pressure at the downstream exit

boundary (y = 200 mm) and side boundaries (x = ±115mm). In contrast, the no-slip boundary condition for velocity was applied to the blades of the hydraulic turbine using the wall function approach. Note that computational grids with arbitrary mesh interface (AMI) were applied along the circular boundary of the interface to represent a rotation of the hydraulic turbine at a fixed tip-speed ratio, which was set at the radial position 59.5mm from the center of the turbine. The time increment was set to 1×10^{-6} s in the numerical simulation, corresponding to a rotation angle of 1.3×10^{-3} degrees at a tip-speed ratio λ = 0.7. This boundary enabled the simulation across the disconnected and adjacent mesh domains. Therefore, the mesh in the domain rotated with the turbine. Because the simulations started with a stationary initial condition, the simulated results showed a transient state in the initial few rotations, depending on the tip-speed ratio. The phase-averaged velocity and torque on the turbine were calculated from the simulation data averaged over 35 cycles of periods once the transient start-up period was concluded. Computational grids of the whole flow field and those of near the blade are shown in Figs. 3-4(a), (b), respectively, for the case of off-axis distance L = 40 mm. It is noted that the nearest grid distance to the blade is δ=10 in wall coordinate.

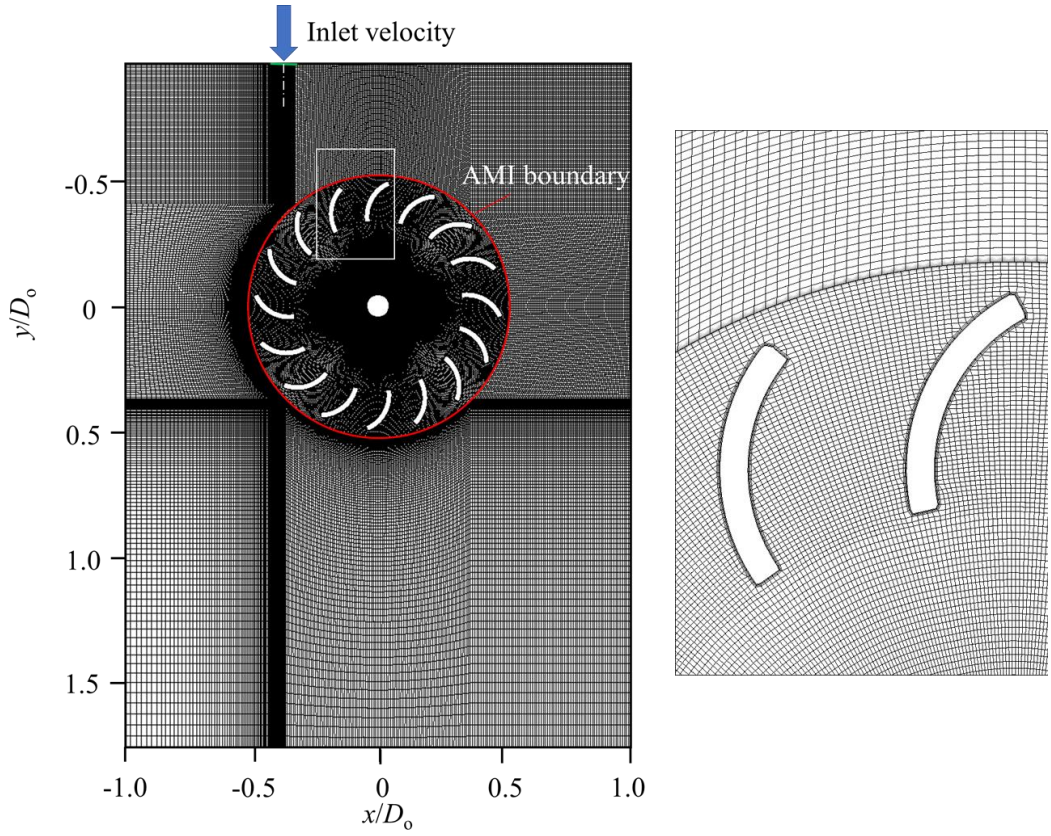

(a) Whole flow fiel (b) Near blade

Fig. 3-4 Computational grids for fluid flow model in and around a waterfall-type cross-flow hydraulic turbine.

3.4 Results and Discussion

3.4.1 Performance of waterfall-type cross-flow hydraulic turbine

Figures 3-5(a) and (b) show a comparison of the experimental results and the numerical simulation for torque coefficient C_t (= $T/(\rho U_e^2 R^2 W)$) and efficiency η (= $T\omega/(\rho g Q H)$), respectively. These results are plotted against the tip-speed ratio λ $(=R\omega/U_e)$, operating at a volume flow rate Q = 0.00153 m^3/s, nozzle exit height H_e = 0.266 m, and off-axis distance L/D_o = 0.35. The experimental torque coefficient C_t decreased gradually with increasing tip-speed ratio λ, while the efficiency η showed a maximum at the median tip-speed ratio and decreased with further increase in tip-speed ratio. The efficiency distribution in the literature is shown for

comparison (Uchiyama et al., 2015), which was carried out at Q = 0.004 m^3/s, H_e = 0.71m and L/D_o = 0.45. Although the efficiency distribution recorded in this study was similar to prior experiments, a substantial difference remains in terms of maximum efficiency and the corresponding tip-speed ratio; the present results recorded a maximum efficiency of 60% at a tip-speed ratio of 0.7, while the results given in the literature were 50% and 0.5, respectively. The improved efficiency in this experiment could be caused by the improved two-dimensionality of the waterfall and the optimization of the off-axis distance L/D_o. In contrast, the present numerical results show a peak efficiency of 66% at λ=0.7, which is slightly larger than that of the experimental results in the present work. This difference between the experimental and numerical efficiencies can be attributed to the scattering of the experimental data and the friction loss of the bearing in the torque measurement, which are included in the upper error bars in Fig.3-5. Note that the upper error bar is larger at a higher tip-speed ratio, reflecting the behavior of friction loss. However, a minor effect of the three-dimensional flow field near the side wall may have contributed to a minor reduction in efficiency. Thus, the present two-dimensional numerical simulation using the VOF method reproduces the experimental performance well within an experimental uncertainty.

Figure 3-6(a) and (b) show the experimental and numerical results for torque and efficiency, respectively, at tip-speed ratios λ = 0.7 of the maximum efficiency, with respect to the off-axis distance L/D_o. The torque and efficiency show a maximum at the middle of the off-axis distance at L/D_o = 0.35 – 0.43, indicating the presence of an optimum off-axis distance. It is observed that the efficiency decreased suddenly for a longer distance L/D_o > 0.46, where the waterfall exited the hydraulic turbine without impinging on the advancing blades. Thus, a decrease in the torque and efficiency is expected for a longer off-axis distance. In contrast, the torque and efficiency decreased at a shorter off-axis distance L/D_o < 0.3, which was caused by the occurrence of

negative torque due to the impingement of the waterfall on the convex side of the advancing blade. Further details of the mechanism are presented in Section 3.4.3. A comparison of the results of the experiment and numerical simulation conducted indicates that the optimum off-axis distance was slightly shifted to a smaller value in the numerical simulation than that observed in the experiment, suggesting the complexity of the flow and torque mechanisms of waterfall-type cross-flow hydraulic turbines.

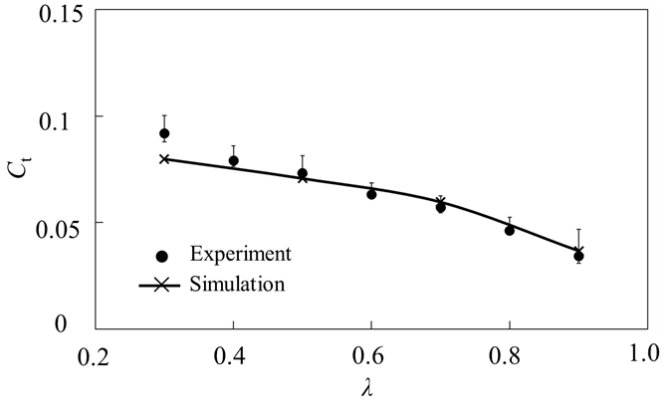

(a) Torque

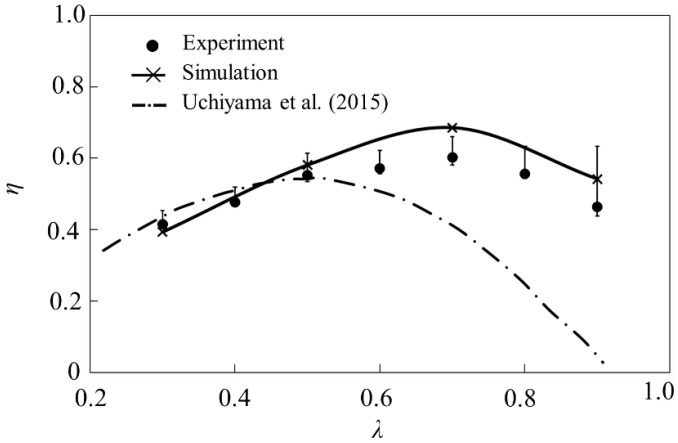

(b) Efficiency

Fig.3-5 Torque and efficiency of waterfall cross-flow hydraulic turbines.

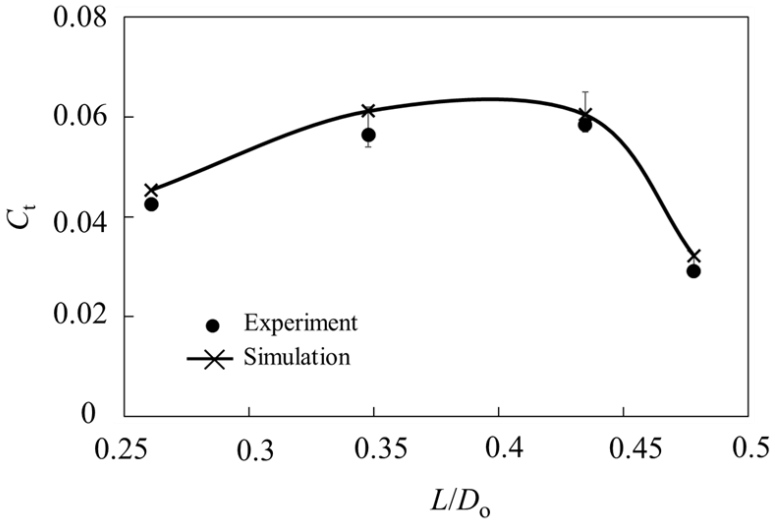

(a) Torque

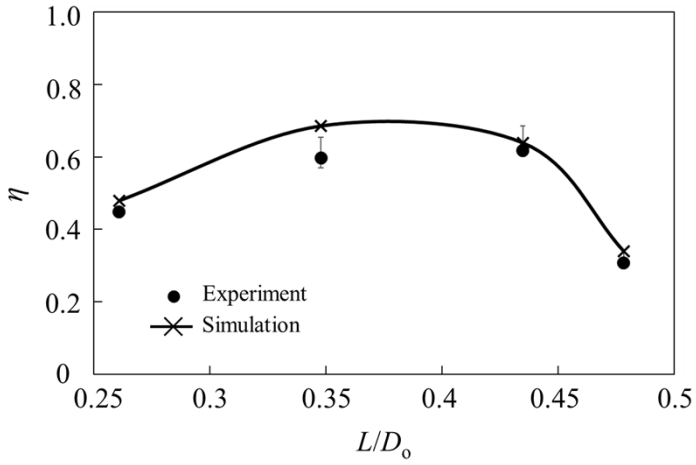

(b) Efficiency

Fig.3-6 Variations of torque and efficiency with off-axis distance L/D_o at $\lambda = 0.7$.

3.4.2 Velocity fields of waterfall-type cross-flow hydraulic turbine

Figures 3-7 and 3-8 show the phase-averaged velocity fields of the waterfall-type cross-flow hydraulic turbine at two different tip-speed ratios $\lambda = 0.3$ and 0.7, respectively, where the off-axis distance was fixed as $L/D_o = 0.35$, with the tip of the 0th blade set to $\theta_b = 0°$. Each figure

shows the phase-averaged PIV measurement (a), and numerical simulation of the water phase (b), as well as those of the air and water phases (c).

The phase-averaged velocity field in Fig.3-7(a) shows a typical velocity field in and around a waterfall-type cross-flow hydraulic turbine operating at a low tip-speed ratio λ = 0.3, which generates a large positive torque caused by the flow impingement on the concave side of the 3rd blade. However, the velocity field shows the flow over the convex side of the 2nd blade, indicating the formation of a Coanda-like flow on the blade contributing to the positive torque acting on the blade in the rotational direction. These flows merge downstream of the 3rd blade near the center of the turbine and generate a high-velocity region toward the concave sides of the 7th and 8th blades. In contrast, the flow directed to the outside of the 3rd blade occurs on the left of the advancing blade, which indicates the occurrence of water flow to the outside of the hydraulic turbine by the slower-moving advancing blades. This results in an increased flow velocity downstream of the advancing blades, as observed in the flow visualization image in Fig. 3-3(a).

The numerical results at λ = 0.3 are shown for the water phase and air and water phase in Fig.3-7(b) and (c), respectively. The results show that as the water flow (b) impinged on the concave side of the 3rd blade, the remainder of the water flow over the convex side of the 2nd blade was directed to the turbine center to impinge on the concave sides of the 7th and 8th blades downstream. Thus, the numerical results agree qualitatively with the PIV measurements. In contrast, the mean velocity field of the air and water phase (c) shows a flow behavior similar to that of the water phase (b), where the water flow entrained the air flow from the surroundings to the inside of the turbine, directing the flow to the 7th and 8th blades. This result indicates that the water-flow-impingement behavior on the 7th and 8th blades was influenced by increased airflow velocity inside the turbine. Note that a recirculating air flow region formed on the

returning blades, where no water flow was present. Thus, airflow behavior may not be neglected when studying the torque mechanism of cross-flow hydraulic turbines, especially near the 7th and 8th blades, where the water flow velocity decreased. It should be mentioned that the velocity field measured by PIV is considered to be a combined velocity field of water and air fluid flow. This is because the target flow field is full of splash caused by the irregularity of the water flow, which follows not only the water phase but also the air phase of the flow.

Figures 3-8(a)~(c) show the mean velocity fields at tip-speed ratio λ = 0.7, where the efficiency of the hydraulic turbine reaches the maximum. These results compare the measured velocity fields by PIV (a), those of the water phase (b), and of the air and water phase (c) obtained from the numerical simulation. Although the measured velocity field at λ=0.7 looks similar to the flow field at a lower tip-speed ratio λ = 0.3 in Fig.3-7(a), the velocity magnitude around the 2nd and 3rd blades was increased at λ = 0.7, as a result of the increased blade velocity of the turbine. This resulted in the growth of the Coanda-like flow over the convex side of the 2nd blade, generating a rotational torque, while the increased blade velocity contributed to a decrease in the rotational torque. The enlarged views of the water velocity field near the 2nd and 3rd blades are shown in Fig. 3-9 for several angles of blade positions θ_b = 45°, 48°, 51°, and 54°, and the sequential growth of Coanda-like flow can be observed with increasing blade angle. These results indicate that a Coanda-like flow is formed over the convex side of the 2nd blade, and the flow separates from the blade downstream. In contrast, the flow through the 2nd and 3rd blades were accelerated downstream of the blades and developed downstream in the hydraulic turbine. This flow developed inclining to the inner side of the advancing blades owing to the influence of increased blade velocity, impinging on the 3rd to 7th blades downstream. Therefore, the flow direction of the cross-flow hydraulic turbine changed with an increase in the tip-speed ratio from λ=0.3 to 0.7. However, the mean velocity on the advancing blade increased over a

wide angle of blade position owing to the increased blade velocity at large tip-speed ratios. As a result, a higher velocity was observed in the wake of the hydraulic turbine downstream of the advancing blades at a large tip-speed ratio.

These changes in the mean velocity field with increasing tip-speed ratio can be explained by the numerical results of the mean velocity field of the water and air-water phases in Fig.3-8(b) and (c), respectively. The mean velocity field of the water flow developed along the advancing blades, resulting in the impingement of the water flow on the 3rd to 7th blades at λ =0.7, which is observed over much wider variation in angles than for the blades at λ =0.3. This indicates that the change in the water flow direction on the advancing blade is caused by the influence of an increased tip-speed ratio. Furthermore, a similar behavior of the mean velocity field is observed in the air-water phase in Fig.3-8(c), which shows an increased mean velocity of air along the advancing blade. Thus, the mean velocity fields of water and air flows show a flow development along the inner advancing blade owing to the increased tip-speed ratio, which may contribute to an increased efficiency of the waterfall-type cross-flow hydraulic turbine at λ = 0.7. It should be mentioned that the air flow field for λ = 0.7 shows an enhanced recirculating flow in the hydraulic turbine, which was induced by the air flow through the returning blades due to the influence of the rotation of the turbine. This flow may have assisted the development of water flow in the hydraulic turbine along the advancing blades because of the increased airflow velocity.

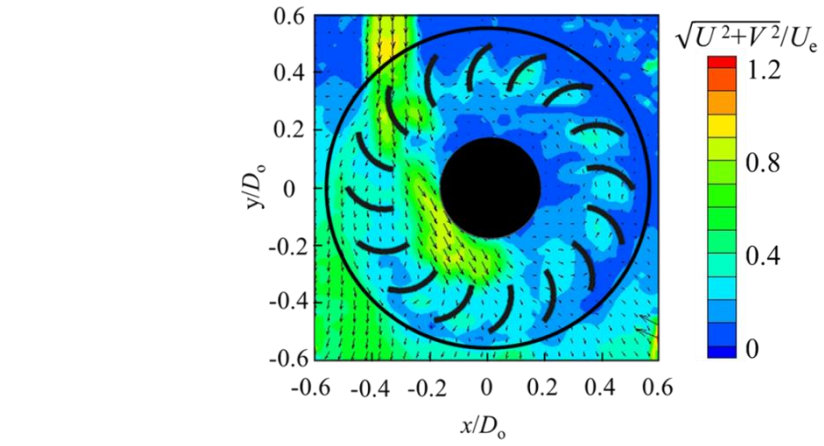

(a) PIV

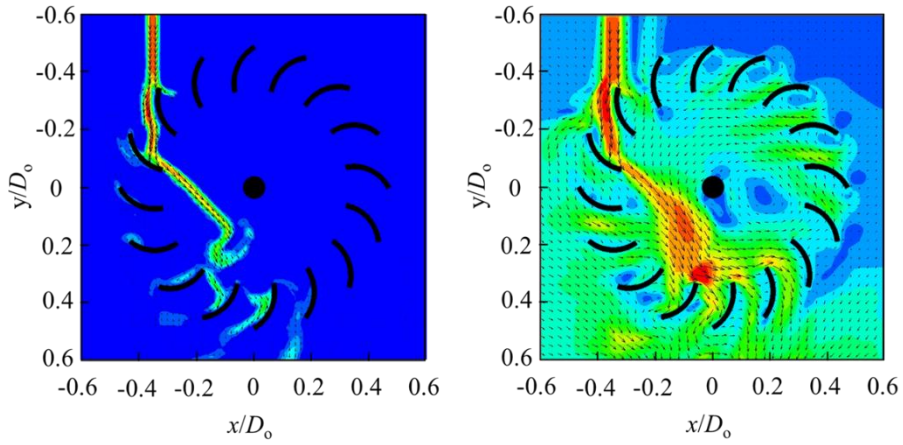

(b) Water phase (Sim) (c) Air and water phases (Sim).

Fig.3-7 Comparison of phase-averaged velocity fields of waterfall-type cross-flow hydraulic turbine at λ=0.3 (L/D_o = 0.35).

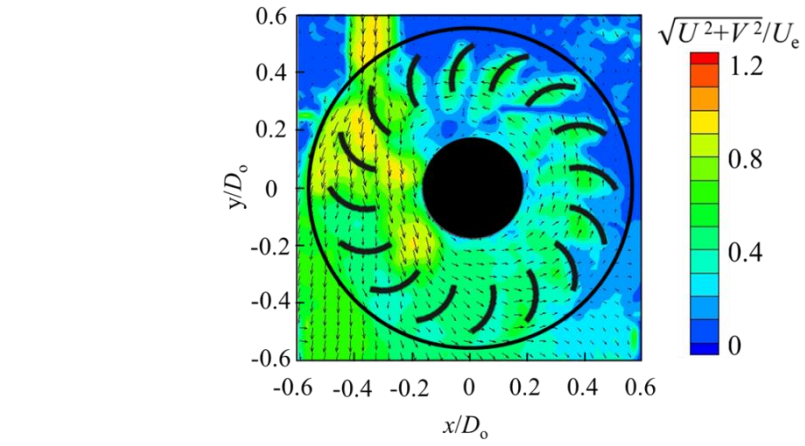

(a) PIV

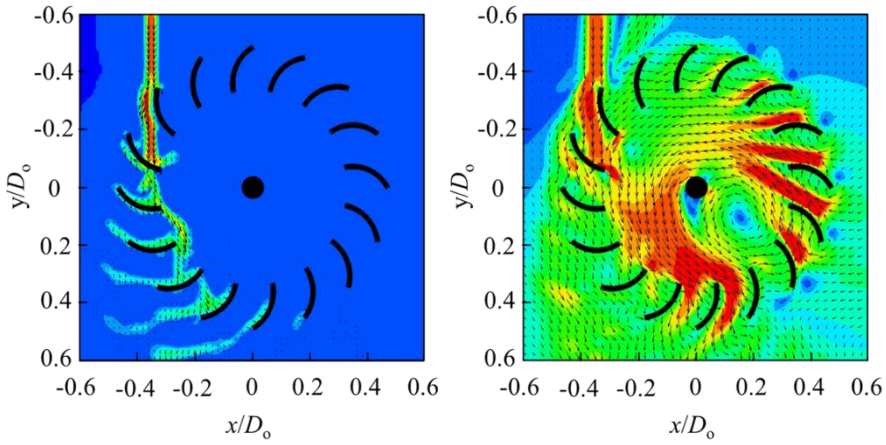

(b) Water phase (Sim) (c) Air and water phase (Sim)

Fig.3-8 Comparison of phase-averaged velocity field of waterfall-type cross-flow hydraulic turbine at λ=0.7 (L/D_o = 0.35).

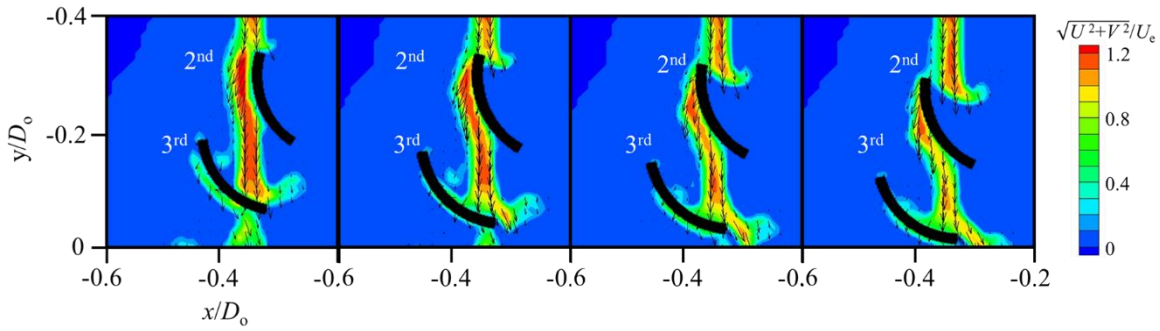

(a) θb = 45° (b) 48° (c) 51° (d) 54°

Fig.3-9 Enlarged views of velocity fields around 2nd and 3rd blades (L/D_o = 0.35, λ = 0.7).

3.4.3 Torque mechanism of waterfall-type cross-flow hydraulic turbine

Figures 3-10 shows the distributions of the local torque coefficient $C_{t\theta}$' on the rotational blades of the waterfall-type cross-flow hydraulic turbine operating at tip-speed ratios λ = 0.3, and 0.7, respectively, for the off-axis distance L/D_o = 0.35, which were obtained from the numerical simulations. The local torque coefficient is defined as $C_{t\theta}' = (rR_1/D_o^2) \cdot \Delta C_p \cdot \cos\varphi$ (ΔC_p: difference of pressure coefficient on the blade, D_o: diameter of hydraulic turbine, R_1 : radius of blade, r: radial distance, φ: blade angle) (Fujisawa and Gotoh, 1994; Wang et al., 2021). The local torque distributions are shown for eight angles of blade position ranging from θ_b = 45° to 202.5° every 22.5°, where the local torque variation is observed. Note that the radial positions r/R=0.7 and 1.0 correspond to the inner and outer edges of the blades, respectively.

The numerical results at a small angle of blade position θ_b =45° show the generation of high rotational torque near the blade tip, which is independent of the tip-speed ratios. This large torque could be caused by the suction pressure of the Coanda-like flow on the convex side of the 2nd blade, which contributes to the rotational torque, as observed in Figs.3-7 and 3-8. With an increase in blade angle to θ_b = 67.5°, the local torque at the outer blade tip suddenly decreases owing to the separation of the Coanda-like flow, while an increase in local torque occurs on the

inner side of the blade, which is caused by the stagnation pressure of the water flow on the concave side of the 3rd blade. The peak magnitude of the rotational torque is slightly higher at large tip-speed ratios, and the peak position is located closer to the inner side of the blade.

With a further increase in angle of blade position to θ_b = 90° to 135°, the local torque decreased and a small magnitude of local torque remains over the 4th to 6th blade. However, a sudden increase in local torque occurs in the middle of the 7th to 9th blades (θ_b = 157.5° to 202.5°) at a small tip-speed ratio λ=0.3, which is caused by the impingement of the accelerated flow through the hydraulic turbine. In contrast, the increased local torque at a large tip-speed ratio λ =0.7 appeared slightly on the outer side of the 7th blade (θ_b = 157.5°), but the local torque magnitude was smaller at λ =0.3. Thus, the increased local torque at large blade angles decreased and the corresponding blade angle also decreased as the tip-speed ratio increases. These results indicate that the variations in the local torque distributions over the blades are consistent with the flow field variations in Figs.3-7 and 3-8.

Figure 3-11 shows the blade-averaged torque distributions at tip-speed ratios λ = 0.3 and 0.7 with the off-axis distance L/D_o =0.35. These distributions reproduce the torque behavior, which is consistent with the local torque distributions in Fig. 3-10. It was found that the blade-averaged torque distributions showed several peaks during the blade rotation, but there were two main peaks at small blade angles and large blade angles, independent of the tip-speed ratios. The former peak at small blade angles was caused by the formation of a Coanda-like flow over the convex side of the blade combined with the impingement of waterflow on the concave side of the advancing blade. This occurred at small blade angles around θ_b = 60° at λ = 0.3, and around θ_b = 70° at λ = 0.7. In contrast, the second peak at large blade angles was caused by the impingement of the accelerating flow on the concave side of the blades downstream at large blade angles. However, the peak magnitudes and the angle of blade position were dependent on

the tip-speed ratios; that is, the magnitudes of the first and second peaks decreased and the second-peak blade angle also decreased with increasing tip-speed ratio. It should be noted that the second peak was smaller than the first, because the impinging flow velocity on the large blade angles decreased in the downstream direction, as observed in Figs. 3-7 and 3-8.

Figure 3-12 shows the blade-averaged torque distributions for various off-axis distances L/D_o = 0.26, 0.35, and 0.43, at a fixed tip-speed ratio λ = 0.7. These results show the presence of several high peaks in the blade-averaged torque distributions dependent on the off-axis distances. Three peaks appeared for the small off-axis distance of L/D_o =0.26, beginning with the negative torque at a small blade angle θ_b = 25° caused by the impingement of waterfall on the convex side of the blade. This was followed by a few positive peaks at blade angles θ_b = 40° to 110°, and a high peak at large blade angles θ_b = 135°. In contrast, the blade-averaged torque distribution at a large off-axis distance L/D_o =0.43 includes two peaks similar to the results of L/D_o =0.35, as shown in Fig.3-11. However, the first peak was significantly increased at θ_b = 90°, and the second peak at θ_b = 180° decreased in comparison with those of L/D_o =0.35. Thus, the number of peaks, peak magnitude, and corresponding angle of blade position varied with varying off-axis distance. As a result, the blade-averaged torque on the cross-flow hydraulic turbine varied with the off-axis distance, and the maximum torque was found near the middle of the off-axis distance L/D_o = 0.35 – 0.43, which qualitatively agrees with the torque measurement in Fig.3-6(a). However, the experimental peak torque in Fig. 3-6(a) is at a larger off-axis distance L/D_o = 0.43. This minor difference between the numerical and experimental results may indicate the difficulty in simulating the complex flow-field behaviors of waterfall-type cross-flow hydraulic turbines in the framework of a two-dimensional numerical simulation with the k-ε turbulence model.

To illustrate the flow field variations of the waterfall-type cross-flow hydraulic turbine examined, the water-phase flow fields are shown in Fig. 3-13 for two different off-axis distances at L/D_o = 0.26 and 0.43. These results indicate that the water flow developed on the advancing blade side at a small off-axis distance L/D_o = 0.26, resulting in flow impingement on the inner blade and the spreading of the flow to the advancing blade side in the downstream. In contrast, the flow field at a large off-axis distance L/D_o = 0.43 shows the flow impingement on the outer blades and its development along the blade at wider blade angles. Thus, the flow field of the waterfall-type cross-flow hydraulic turbine was significantly altered by the influence of off-axis distance.

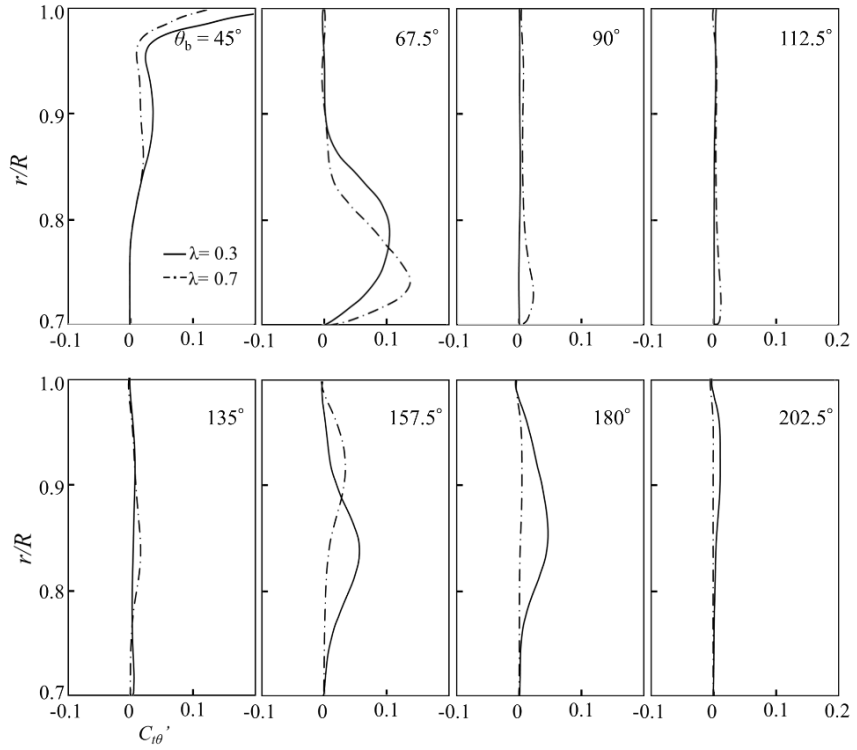

Fig.3-10 Local torque distributions for various blade angles θ_b (L/D_o = 0.35).

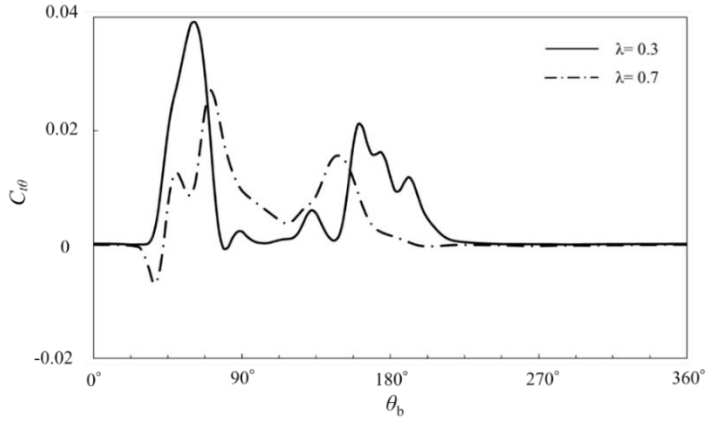

Fig. 3-11 Variation of blade-averaged torque coefficient $C_{t\theta}$ with the blade angle θ_b (L/D_o = 0.35).

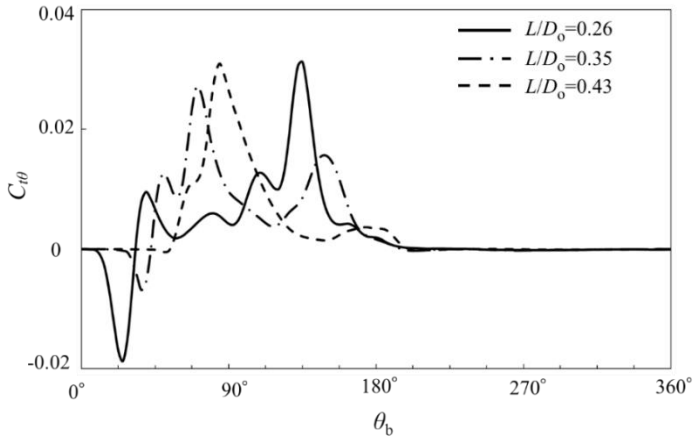

Fig. 3-12 Variation of blade-averaged torque coefficient $C_{t\theta}$ with the off-axis distance L/D_o (λ=0.7).

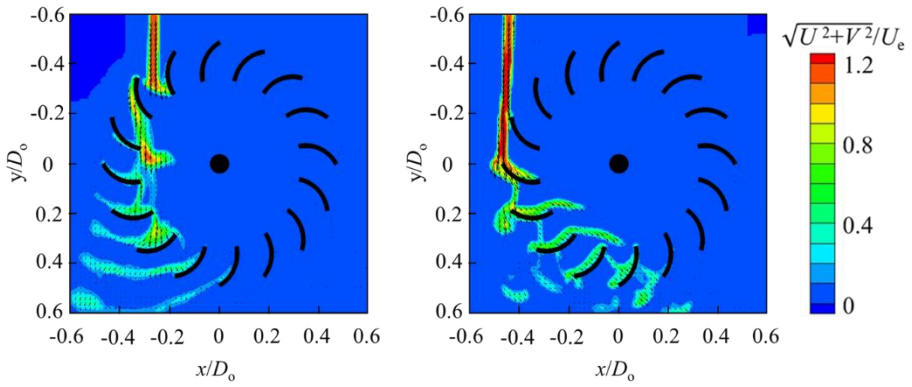

(a) L/D_o =0.26 (b) L/D_o =0.43

Fig. 3-13 Phase-averaged velocity fields of water phase (λ = 0.7).

3.5 Conclusions

The performance of a waterfall-type cross-flow hydraulic turbine was studied both by experiment and by numerical simulation. The experimental study was carried out by measuring the torque and efficiency of a cross-flow hydraulic turbine in a two-dimensional waterfall, and the flow field in and around the hydraulic turbine was measured by phase-averaged PIV. Furthermore, these results were compared with a two-dimensional numerical simulation using the VOF method for two-phase flow analysis.

The experimental results showed a maximum power efficiency of 60 % at a tip-speed ratio of 0.7, which was higher than the measured efficiency of 53 % reported in the literature. This increased efficiency was reproduced by a two-dimensional numerical simulation using the experimental inlet velocity, and the peak efficiency reached 66 %. This result suggests the validity of the numerical result using the VOF method for the prediction of two-phase flow of a waterfall-type cross-flow hydraulic turbine.

To understand the flow and torque mechanisms of such turbines, a comparative study was carried out using the phase-averaged PIV measurements and the numerical simulations in and

around the cross-flow hydraulic turbine. It was found that the measured velocity field featured a Coanda-like flow on the convex side of the advancing blade at small blade angles and flow impingement on the concave side, which merged to form an accelerating flow through the hydraulic turbine toward the downstream blades at large blade angles. Furthermore, the flow fields of the water and air flows were separately studied in the numerical simulation to understand the torque mechanism of water flow behavior, and the airflow within the turbine was found to assist the water flow behavior.

These flow variations were well reproduced in the local torque generation and blade-averaged torque variations with the angle of blade position, which resulted in the first and second peaks of torque distribution at small and large blade angles, respectively. The major torque was generated at small blade angles, while a certain magnitude of torque occurred at large blade angles, resulting in an optimum off-axis distance value for the torque and efficiency of the waterfall-type cross-flow hydraulic turbine studied.

References

Adhikari, R.C., & Wood, D. (2018a) The design of high efficiency crossflow hydro turbines: A review and extension. Energies, 11, 267 (18 pages).

Fujisawa, N., & Gotoh, F. (1994) Experimental study on the aerodynamic performance of a Savonius rotor. ASME J. Solar Energy Engineering, 116, 148-152.

Fujisawa, N. (1996) Velocity measurements and numerical calculations of flow fields in and around Savonius rotors. Journal of Wind Engineering and Industrial Aerodynamics, 59, 39-50.

Fujisawa, N., Takeda G., & Ike, N. (2004) Phase-averaged characteristics of flow around a circular cylinder under acoustic excitation control. Journal of Fluids and Structures, 18, 159-170.

Fujisawa, N., Yamagata, T., Hayashi, K., & Takano, T. (2012) Experiments on liquid droplet impingement erosion by high-speed spray. Nuclear Eng. Design, 250, 101-107.

Ikarashi, Y., Uno, T., Yamagata, T., & Fujisawa, N. (2018) Influence of elbow curvature on flow and turbulence structure through a 90° elbow. Nuclear Engineering and Design, 339, 181-193.

Kiuchi, M., Fujisawa, N., & Tomimatsu, S. (2005) Performance of PIV system for combusting flow and its application to spray combustor model. Journal of Visualization, 8, 269–276.

Nishi, Y., Inagaki, T., Li, Y., Omiya, R., & Fukutomi, J. (2014a) Study on an undershot cross-flow water turbine. Journal of Thermal Science, 23, 239-245.

Nishi, Y., Inagaki, T., Li, Y., Omiya, R., & Hatano, K. (2014b) The flow field of undershot cross-flow water turbines based on PIV measurements and numerical analysis. International Journal of Fluid Machinery System, 7, 174-182.

Sammartano, V., Aricò, C., Carravetta, A., Fecarotta, O., & Tucciarelli, T. (2013) Banki-Michell optimal design by computational fluid dynamics testing and hydrodynamic analysis. Energies 6, 2362-2385.

Uchiyama, T., Uehara, S., Fukuhara, H., Iio, S., & Ikeda, T. (2015) Numerical study on the flow and performance of an open cross-flow mini-hydraulic turbine. Proceedings of the IMechE Part A, Journal of Power and Energy, 229, 968-977.

Wang, T., Shikama, H., Yamagata, T., Fujisawa, N. (2019) Experimental and numerical studies on flow field around an undershot type cross-flow water turbine. Proc. 16th Int. Conf. Fluid Dynamics, Sendai, OS13-10 (2 pages).

Wieneke, B, (2015) PIV uncertainty quantification from correlation statistics. Measurement Science and Technology, 26, 074002 (10 pages).

Chapter 4 Concluding remarks

In this thesis, the flow mechanism and the performance of the open cross-flow hydraulic turbine in underflow and waterfall operating conditions were studied both experiment and numerical simulation. To understand the flow mechanism of the hydraulic turbine experimentally, the phase-averaged PIV measurements were introduced to the flow field and the performance of the hydraulic turbine was studied experimentally. On the contrary, the flow and the performance of the hydraulic turbine were studied by two-dimensional numerical simulations using VOF method. These studies can be summarized as follows.

1. The flow field in and around the open cross-flow hydraulic turbine in an underflow operating condition were examined by PIV measurement and numerical simulation, and the results agreed relatively well with each other. These results indicated that the flow-field showed the accelerated flows over the blade at large blade angles in the downstream, which highly contributed to the torque generation of the hydraulic turbine. These flows together with the flow between the turbine and the bottom wall were accelerated by the clearance effect between them, and the performance of the hydraulic turbine is improved by optimizing the clearance. This resulted in 39% in efficiency in numerical result, which is higher than that of the literature.
2. The flow fields in and around the waterfall cross-flow hydraulic turbine were studied by PIV measurement and numerical simulation, and the results agreed relatively well with each other. The results showed that the formation of Coanda-like flow on the convex side of the blade and the flow impingement on the concave side of the blade. They contributed to torque generation of the hydraulic turbine, similar to the result of

underflow operating condition. However, the additional torque generation mechanism was observed in the waterfall operating condition, which was the impingement flow from the advancing blade to the returning blade. It was found that the offset distance is another influential parameter on the performance of the waterfall cross-flow turbine, and the turbine efficiency was improved by the optimization. This optimization improved the efficiency up to 60%, which was larger than the previous experimental result for waterfall operation and that of the underflow operation in the literature.

3. Regardless of the operating conditions of open cross-flow hydraulic turbine, the basic mechanisms of the torque generation were the same for underflow and waterfall types of cross-flow hydraulic turbine. The rotational torque was generated by the Coanda-like flow on the convex side of the blade and the flow impingement effect on the concave side of the blade on the advancing blade. However, the extra torque occurred on the large blade angles of the hydraulic turbine by the flow impingement effect of the outflow from the advancing blade to the returning blade. This was because of the geometrical advantage of the waterfall type cross-flow hydraulic turbine. The other advantage of the waterfall-type cross-flow turbine was the variable offset distance of the flow impingement position on the advancing blade. Therefore, the improved efficiency of the waterfall-type cross-flow hydraulic turbine came from the optimization of these additional parameters. See appendix for the comparison of the efficiency for two types of cross-flow hydraulic turbine at the same definition of water head ΔH ($=H_u - H_d$). However, there might be a space for further improvement of cross-flow hydraulic turbine by optimizing the guide-vane position of the hydraulic turbine and the blade-shape profiles. These factors will be important topics of research in future.

Appendix

Table. The performance of the cross-flow hydraulic turbine under two operating conditions with ΔH, when the power coefficient is maximum.

	H_u(mm)	H_d(mm)	ΔH(mm)	C_t	$\eta_{\Delta H}$
Underflow type (λ=0.85 and H_b = 17.5mm)	65	60	5	0.6261	0.3354
Waterfall type (λ=0.7 and L = 40mm)	266	-57.5	323.5	0.0596	0.5316

Acknowledgements

This research was financially supported by Niigata University. The author would like to express gratitude to my supervisor of Professor Emeritus Nobuyuki Fujisawa of Niigata University for the helpful suggestions on this research. The helpful suggestions are acknowledged to Mr. Takayuki Yamagata of Niigata University. The author also express thanks to Professors Kazuhiro Hiramoto, Koji Matsubara, and Atsushi Sakurai for their encouragements and suggestions in preparation of final version of the PhD thesis. Furthermore, I would like to thank Mr. S. Liu for his help in designing the cross-flow hydraulic turbine in the preliminary study. I would like to thank to Mr. H. Shikama for his help in developing the experimental technique and facilities for the underflow-type cross-flow hydraulic turbine, and experimental data and analysis from the waterfall-type cross-flow hydraulic turbine. Lastly, I would like to thank my parents for supporting me during the course of my study.